Eindhoven University of Technology

BACHELOR

Investigating the relation between linear and nonlinear zonal flow response in Wendelstein 7-X

van Hoof, Emma

Award date:
2019

Link to publication

EINDHOVEN UNIVERSITY OF TECHNOLOGY

Department of Applied Physics
Science and Technology of Nuclear Fusion

Investigating the relation between linear and nonlinear zonal flow response in Wendelstein 7-X

Final Bachelor Project

E.M.T. van Hoof

1021471

Supervisors:
dr. J.H.E. Proll
MSc. C.D. Mora Moreno

Eindhoven, June 2019

Abstract

Turbulent transport is the next big challenge in optimized stellarators, since it limits energy confinement. The characteristics of turbulent transport can be described by the heat fluxes and related transport coefficients. Having a model for the heat flux would be helpful to measure the performance of a magnetic geometry without the need for expensive simulations. A reduced model originally designed for the Large Helical Device (LHD) stellarator [19] relates the Ion Temperature Gradient (ITG) generated turbulence and zonal flows as a saturation mechanism; with the final goal of predicting the heat diffusivity. The coexistence of ITG-generated turbulence and zonal flows is well established in tokamaks. After the implementation of the model on the geometry of stellarator Wendelstein 7-X, the model has to be reduced. There has been found a linear relation between linear and nonlinear simulations of turbulence, from which the coefficient can be used to reduce the model. For zonal flows such a relation has not been established. Therefore we aim to investigate different characteristics of the linear zonal flow response that represent the nonlinear zonal flow strength. Such characteristics are identified and compared against functions of the nonlinear turbulent spectrum and the nonlinear zonal flow strength. The data that is used is retrieved using the GENE code. The characteristics identified are the residual value, the zonal flow decay time, the integrals over the real and imaginary part, the angular frequency and the decay constant. No relations have been found between the identified characteristics and nonlinear simulations of turbulence and the zonal flow response in Wendelstein 7-X. The identified characteristics and the used functions of the nonlinear turbulent spectrum and the nonlinear zonal flow strength are found to be not adequate for determining such a relation.

Contents

Chapter 1

Introduction

The excessive use of fossil fuels has created two major problems on a global scale. The first is that the world's temperature is rising due to the excess amount of greenhouse gasses that are emitted by burning fossil fuels. This results in climate change and causes problems such as loss of biodiversity, rising of the sea level, dehydration of land, amongst others. The second major problem is that humankind is running out of reliable and big-scale energy sources. The timeline shown in Figure 1.1 represents a time scale of the fast consumption of fossil fuels during the history of humankind. Fossil fuels are produced when enormous pressures are exerted on organic materials. Over a long period of time, these pressures let the organic materials form into oil, gas or coal. Such period of transformation falls in a bigger time scale than the one presented in Figure 1.1, showing that these fuels are consumed in just a fraction of this time. This has motivated the research for different sources of energy for a sustainable future, especially since human civilization is continuously expanding and demanding more energy than ever before. A promising energy source is seen in nuclear fusion, which is discussed in the next section.
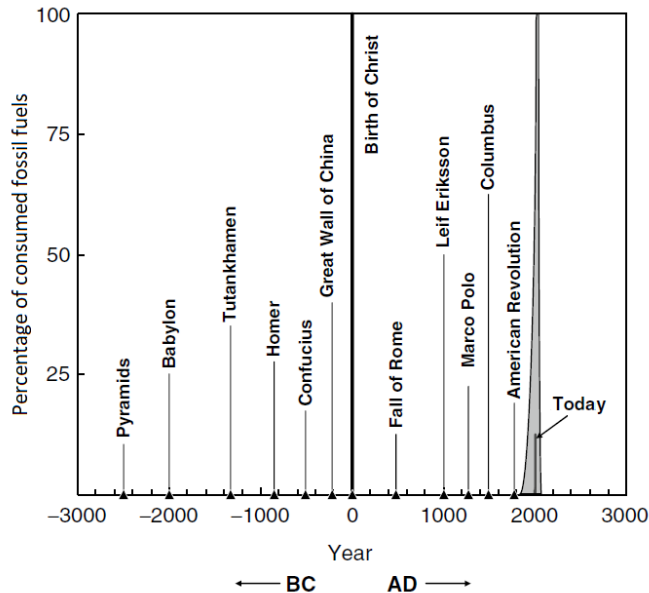

Figure 1.1: Time scale of the fast consumption of fossil fuels during the history of humankind. The grey area refers to the time in which all fossil fuels present on earth are consumed. Adapted from [2].

1.1   Nuclear Fusion

The nuclear reaction of fusion requires high-velocity nuclei to fuse together, releasing energy in this process. The most common fuels of fusion reactors are deuterium and tritium, which are two isotopes of hydrogen. When they fuse they form a helium nucleus and a neutron. Helium has a bigger binding energy per nucleon than deuterium or tritium. This difference in binding energy before and after the fusion reaction gets released as kinetic energy of the reaction products [5]. For fusion to occur, the deuterium and tritium nuclei are required to have enough energy to overcome the Coulomb forces repelling each other. This is why fusion only occurs at high temperatures. In a fusion reactor a temperature of over $100,000,000$ K is required [2]. At this temperature, particles are ionized into a plasma. A more detailed description of magnetized plasma physics is given in section 2.1.

Nuclear fusion is envisioned to have significant advantages. One is fuel availability: The initial fuels can be obtained from sea water and lithium deposits. Deuterium is present in sea water and can be extracted from it. One way in which tritium can be bred is by a nuclear reaction between neutrons and lithium within the fusion reactor. There is enough sea water and lithium present to use for fusion energy for at least 9.4 million years, taken the current average annual energy consumption into account [21]. Furthermore, in contrast with nuclear fission, the fusion reaction cannot lead to an uncontrolled chain reaction, it has a reduced risk of proliferation and the waste products are not radioactive, but activated [21].

However, after more than fifty years of research fusion energy is still not a mature technology. The main cause of this is that a fusion reactor is a very complex system and the engineering is not sufficiently advanced as to build a reactor that can produce energy more than it needs. A fusion reactor needs a significant amount of energy for energy and particle confinement. Due to the high temperatures of the plasma, it is nearly impossible to find a material that can provide confinement in direct contact with the plasma and withstand melting [2].

The research of fusion energy has been advanced using magnetic confinement devices. In these devices the plasma particles are kept in place through the Lorentz force

$$\boldsymbol{F_L} = q_i(\boldsymbol{E} + \boldsymbol{v_i} \times \boldsymbol{B}). \tag{1.1}$$

Here, q_i is the charge of particle of species i, $\boldsymbol{E}$ is the electric field, $\boldsymbol{v_i}$ is the velocity of particle of species i and $\boldsymbol{B}$ is the magnetic field. In general, particles move in the direction of electric and magnetic field lines [5]. When they have a velocity perpendicular to the magnetic field lines, the Lorentz force makes them deflect towards these field lines. As a result, particles gyrate around magnetic field lines in the plasma [2]. The center of the orbit that the particles are following, is defined as the guiding center. The radius of the orbit is defined as the Larmor radius defined by

$$r_L = \frac{m_i v_\perp}{|q_i| B}, \tag{1.2}$$

where $v_\perp$ is the speed of the particle perpendicular to $\boldsymbol{B}$ and B is the magnetic field strength. Consequently, the Larmor radius varies for different particles since it depends on the mass, velocity and charge of the particle. In a fusion reactor the magnetic field lines are closed. Particles following these lines are thus confined. Coils inducing magnetic fields are used in these devices to produce the required magnetic field.

The most common type of fusion reactors is a tokamak. These reactors are characterised by an axi-symmetric toroidal chamber, a torus, where the plasma is moving in the toroidal direction, shown in Figure 1.2. The toroidal direction is the φ-direction, visualized as well in Figure 1.2. Coils in the poloidal direction are needed to produce the toroidal magnetic field that is required to confines the particles. The poloidal direction is the θ-direction, as well visualized in Figure 1.2.

The poloidal coils are closer to each other in the middle of the torus and less closer to each other on the outside. Consequently, the magnetic field on the inside of the torus is stronger than on the outside. Due to this, the Larmor radius decreases on the inside and increases on the outside of the torus. This causes a drift, called the ∇B-drift, for positively charged particles downwards and
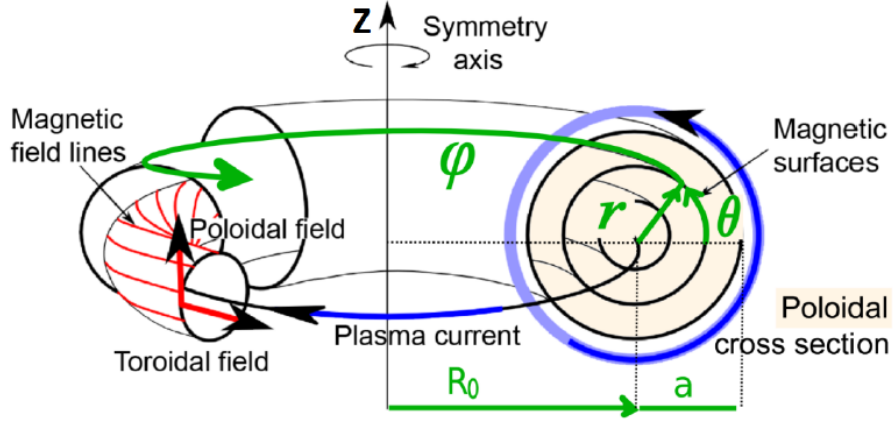
Figure 1.2: Magnetic configuration of a tokamak, visualizing the magnetic field lines and magnetic surfaces, the plasma current, the coordinates r, θ and φ, the major radius R_0 and minor radius a and the poloidal and toroidal fields [7].

for negatively charged particles upwards [2]. This is shown in Figure 1.3. The charge separation produces an electric field in the vertical direction. In the presence of an electric field, plasma particles will move slowly outwards by effects of the $\boldsymbol{E} \times \boldsymbol{B}$ drift. The ∇B-drift, $\boldsymbol{E} \times \boldsymbol{B}$ drift and other guiding center drifts that play a role in fusion devices are explained in section 2.1.
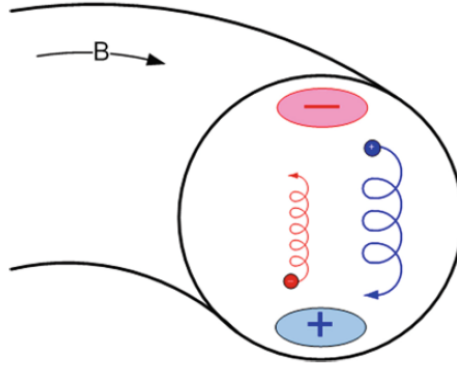
Figure 1.3: Due to the difference in magnetic field strength on the inside and outside of the torus, the Larmor radius decreases on the inside and increases on the outside, which causes a drift for positively charged particles downwards and for negatively charged particles upwards [2].

To compensate for the described charge separation effect, the net magnetic field in the torus needs to be helically twisted, in such a way that the charge separation is averaged out when the plasma completes one whole turn in the toroidal direction [2]. The degree of twisting is measured by the rotational transform

$$\frac{\iota}{2\pi} = \frac{1}{2\pi} \frac{\Delta \theta}{\Delta \varphi}, \tag{1.3}$$

which defines the poloidal displacement of the magnetic field line when it has completed one whole turn in the toroidal direction. To produce the helically twisted magnetic field, besides the toroidal magnetic field also a poloidal component is needed. In a tokamak, this particular field can be

achieved by a toroidal current in the plasma. This current is generated using the plasma as the secondary winding of a transformer [5].

A different principle to generate a twisted magnetic field is used in stellarators. Stellarators are also torus shaped fusion reactors, where specific coils only produce the confining helical magnetic field. Therefore, stellarators do not need a toroidal current in the plasma. More on stellarators is discussed in the next section.

1.2 Stellarators

Stellarators are potential future power plants. They can operate in a steady state since they do not need an induced toroidal current like tokamaks do to produce the helical magnetic field needed to confine the particles [22]. In contrast to tokamaks, stellarators use complex coils to produce this required field. Due to these complex coils, stellarators are generally non-axisymmetric and this makes their geometry significantly more complex than that of tokamaks. The degrees of freedom involved in stellarator geometries affect the performance of the plasma in many different aspects, therefore, every configuration has different properties. In Figure 1.4, stellarator Wendelstein 7-X (W7-X) is shown, which is the largest stellarator build, located in Greifswald, Germany. The blue shapes represent the complex coils needed to confine the plasma.

The first configuration of W7-X was the Standard Configuration. To gain knowledge of the influence of the geometry on the plasma physics in W7-X, several different configurations were investigated by Geiger et al. [11]. These configurations are named: Standard, High Mirror, Low Mirror, High Iota and Low Iota; and they are obtained by adjusting the coils in certain ways. High and Low Mirror refer to the presence of magnetic mirrors in the stellarator. Magnetic mirrors are discussed in section 2.1. High and Low Iota differ in strength of the rotational transform $\iota/2\pi$ [11]. The research described in this report is conducted using simulation data based on these five configurations of W7-X. Configurations can also differ in the global magnetic shear that plays a role in the plasma. The global magnetic shear for the five configurations found at different normalized radii s is shown in Figure 1.5. s is defined as the normalized radius in radial direction of the poloidal cross-section shown in Figure 1.2. Thus, this is a number between 0 and 1 representing the fraction of the minor radius a.

In stellarators the risk of disruptions that cause turbulence is low [8]. In contrast, tokamaks need plasma currents to maintain confinement, which affects the macroscopic stability of such devices and increases the risk of disruptions. Despite stellarator macrostability, free sources of energy like temperature and density gradients promote the growth of microinstabilities; which through nonlinear interactions result in turbulent transport and lose of energy confinement. Turbulence is discussed in the next section.
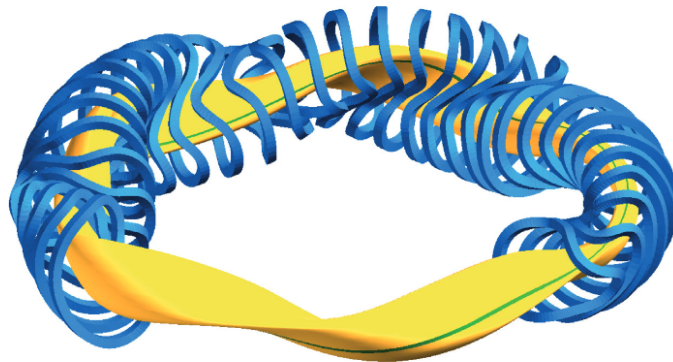

Figure 1.4: Configuration of stellarator Wendelstein 7-X. The yellow region represents the plasma, the blue shapes represent the coils and the green line represents a magnetic field line [9].
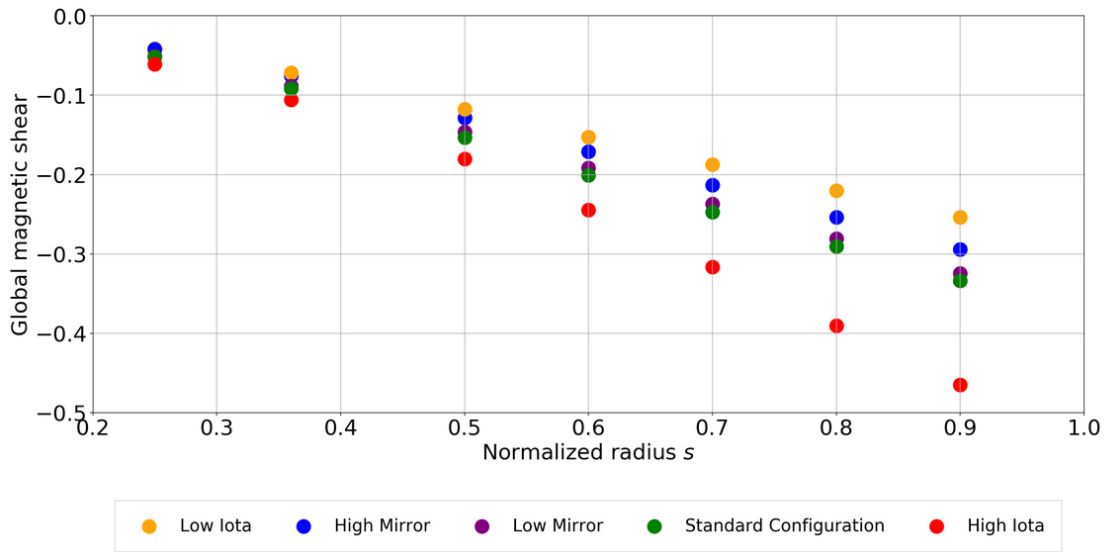
Figure 1.5: The global magnetic shear plotted against the normalized radius s for all configurations.

1.3 Turbulence

Turbulence plays an important role in fusion reactors since it limits energy and particle confinement [10] [22]. Turbulent flows are unpredictable, chaotic and hard to control. A big part of the fusion research focuses on understanding and controlling turbulence arising in the microscopic scales.

Turbulence is studied as the nonlinear interaction of multiple instabilities. Instabilities arise when small perturbations in the plasma lead to bigger perturbations. Due to this, turbulence is unpredictable: any small perturbation can cause totally different behaviour than another [18]. In plasmas, instabilities are caused by gradients in for instance temperature or density, as well as geometric characteristics. Gradients provide free energy sources for instabilities [18]. The steeper the gradients are, the more free energy is available and the more the instabilities will grow. In general, gradients are steeper at the edge of the plasma, where the plasma ceases to exist. Instabilities are also driven at the edge of the plasma since that is a region of so called 'bad curvature'. In this region perturbations get suppressed less fast as in the centre of the plasma. An example of an instability that can lead to turbulence is the Ion Temperature Gradient (ITG) instability that will be discussed in section 2.2.

In turbulent flows, structures exist that are called eddies [18]. They are structures consisting of collections of particles that twirl together in vortices. The largest eddies determine the macro-structure of turbulence, whereas the smallest eddies determine the micro-structure of turbulence [18]. The dynamics at these scales is described in their own length, velocity and timescale. Bigger eddies can drift further outwards and can therefore transport energy further outwards. This decreases energy confinement in fusion reactors, while big eddies break up into smaller eddies and lose their energy. This is called the energy cascade [18]. When the eddies are so small that they are in the micro-scale, their energy gets dissipated into heat [18]. Zonal flows play a big role in shearing turbulent eddies and breaking them up into smaller ones. In this way zonal flows suppress turbulence and also decrease energy transport. Zonal flows are discussed in the next section

1.4 Zonal flows

Zonal flows are present in toroidal devices as band-like shear flows in the poloidal direction [4]. Two bands next to each other flow in opposite directions, their direction depending on the radial coordinate [4]. This is shown in Figure 1.6. Over the whole poloidal turn their velocity is constant.

Zonal flows arise due to turbulence. Turbulent energy is converted to energy for zonal flows when the shearing of the zonal flows takes this energy from the turbulent eddies. Zonal flows cannot use free energy directly, so they receive energy only via turbulent stress [14].

Zonal flows have been observed to regulate and suppress turbulence in tokamak plasmas, in simulations as well as in experiments [16] [10]. Plasma eddies that flow between the zonal flow bands get sheared and stretched by the zonal flows. Eventually, this tears the eddies apart and turbulence levels are reduced.

Since zonal flows also exist due to turbulence, the turbulence-zonal flow system has been also modeled as a predator-prey system [4]. In this predator-prey system, energy is exchanged between micro instabilities in the plasma and zonal flows [4] [14]. The total energy is conserved. Since turbulence is reduced by the zonal flows, the zonal flows damp eventually.

In the next section, the purpose of the research that is discussed in this report will be explained.

Figure 1.6: Zonal flows in a toroidal geometry. The arrows denote the flow directions. Adapted from [4].

1.5 The purpose of this research

Research on turbulence in fusion plasmas is important since turbulence reduces energy and particle confinement. Turbulence in plasmas is computationally simulated and models are developed to gain understanding of the phenomena experimentally observed. In simulations kinetic equations describing the dynamics of the particles are solved. Each particle has six degrees of freedom, three for its position and three for its velocity. Making use of the so called gyrokinetic equations reduces the number of dimensions needed to describe the plasma particles. This is explained in section 2.1. Still, many dimensions are needed and this makes the equations difficult to solve. It is also computationally expensive to run nonlinear simulations [19]. Linear simulations, where the nonlinear terms in the equations are neglected, are used to approach the characteristics of turbulence while minimizing computational costs. To understand more of energy confinement, predicting the heat flux of the plasma is desired. The heat flux is related to the ion heat conductivity χ_i, but also to present instabilities that feed turbulent fluctuations. Since simulating is still very expensive, the use of models can be very beneficial. Nunami, Watanabe and Sugama describe in their paper *A reduced model for ion temperature gradient turbulent transport in helical plasmas* a model made to predict χ_i via linear simulations of turbulent transport due to the ion temperature gradient (ITG) instability and linear simulations of zonal flows [19]. Form now on, this model will be referred to as 'Nunami's model'. In this model, the relations between linear and nonlinear simulations of both turbulence and zonal flow response are used to make predictions of the heat conductivity.

Nunami's model shows that it is possible to use linear data to predict nonlinear simulation results [19]. The model is build for the Large Helical Device (LHD), a stellarator quite different

from W7-X. Using Nunami's model on simulation data based on configurations of W7-X does not reproduce the same relation between linear and nonlinear zonal flow response as found for the LHD in Nunami's model. It is not clear how the nonlinear zonal flow response is related to the linear one for W7-X. Therefore, this report discusses research done on finding the right characteristic of the linear zonal flow response that represents the nonlinear zonal flow strength for W7-X. Using linear simulation data of the five configurations of W7-X discussed above, the linear zonal flow response is observed and patterns in the behaviour of it are described. From this, several characteristics of the linear zonal flow response are identified and quantified. These characteristics are then related to nonlinear data. A conclusion is drawn on whether there is found a relation between linear and nonlinear zonal flow response or not. This research is useful in order to find a reduced model for W7-X derived from Nunami's model for the LHD.

1.6   Outline of this report

The outline of this report is given to conclude this chapter. In chapter 2, a theoretical background on plasma physics, turbulence, the ITG instability, simulating turbulence and zonal flows is discussed. Nunami's model is discussed. In chapter 3, the research objectives and methods are described. In chapter 4, the results are presented. The behavior of the linear zonal flow response is described and the characteristics of the linear zonal flow response are quantified and related to nonlinear data. The relations found between linear and nonlinear data are here presented and discussed. Finally, in chapter 5 a conclusion is drawn and future research is discussed.

Chapter 2

Theoretical background

Before proceeding to the research and results, it is important to review some theoretical background. First, some plasma physics will be discussed. A more detailed account of single particle motion in magnetized plasmas and of gyrokinetic theory is given. Secondly, a more detailed account of the role of the ITG instability and simulating turbulence is given. Finally, Nunami's model is discussed in more detail.

2.1 Plasma physics

A plasma is a gas with such a high temperature that the atoms in it get ionized. Ionization arises when collisions between the atoms happen at such a high energy that due to the collision an electron gets excited and leaves the electron-shell it occupies [1]. Consequently, a plasma consists of positively charged ions and negatively charged electrons.

Plasmas have important properties. The charged particles cancel applied electric fields since oppositely charged particles that are present in the plasma will shield off applied charges. In that way they provide an opposite field. A plasma behaves thus as a dielectric material. Due to this shielding, the plasma will stay quasi-neutral because there will not exist large electric potentials or fields in it that make positive and negative charges separate [1].

An other property important to keep in mind is that the particles influence each other at larger distances. This is due to the electric and magnetic fields that arise due to their charge and motion, which are dependent on distance [1].

Furthermore, there can be many different temperatures present in a plasma. This also means that particles can have many different velocities. These arise due to differences in net force acting on the particles, depending on position or direction. Electrons and ions in general have different temperatures T_e and T_i, due to the difference in collision rate between two ions, two electrons or an ion and an electron. These temperature differences play a huge role in the ion temperature gradient instability discussed in section 2.2. But first, more is explained about single particle motion in a plasma.

Single particle motion in a plasma

Although in a fusion plasma huge numbers of particles are present, it is useful to know the principles behind single particle motion. A charged particle reacts to electric and magnetic fields. As explained in the introduction, charged particles will gyrate around magnetic field lines. The motion of the particles will be in the direction such that the magnetic field arising from the motion of the particle itself is directed opposite to the direction of the applied magnetic field. Thus, a plasma is not only dielectric but also diamagnetic; plasma particles try to cancel applied magnetic fields. The resulting total motion of charged particles due to the effects of both electric and magnetic fields are helical motions around the magnetic field lines [1]. The particles' motion

changes when the magnetic or electric fields are nonuniform. A more detailed account of single particle motions due to nonuniform fields is given in the next paragraphs.

When the magnetic field strength differs in space and the difference in $\boldsymbol{B}$, ∇B, is perpendicular to the direction of $\boldsymbol{B}$ itself, a so called grad-B drift will arise. Since the Larmor radius is proportional to B, it increases when the particle is moving in a stronger magnetic field and decreases when it is in a weaker magnetic field. Consequently, the guiding center will drift perpendicular to the direction of ∇B and $\boldsymbol{B}$ [1]. This is visualized in Figure 2.1. This is what is happening in a torus shaped fusion reactor when there is no poloidal magnetic field present, as explained in the introduction. Drifts arising due to a dependence on the Larmor radius are called finite-Larmor-radius effects. These effects can cause instabilities in plasmas, which are called drift instabilities or micro-instabilities [1].
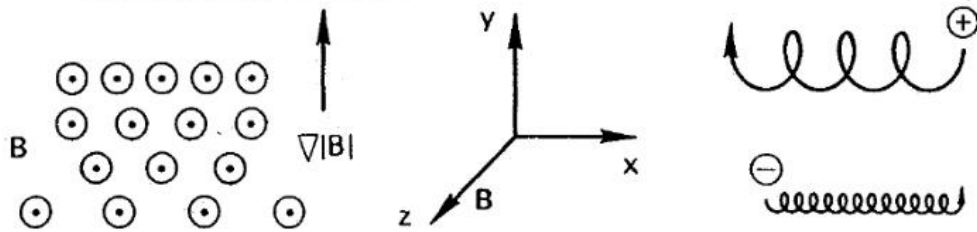

Figure 2.1: ∇B-drift of positive and negative charged particles in a nonuniform magnetic field [1].

An other drift due to non-uniformity of the magnetic field can arise due to curved field lines. Magnetic fields in fusion reactors are curved into a helix. This curvature leads to a guiding center drift owing to the centrifugal force acting on particles that follow the field lines. This force is directed perpendicular to the field lines and therefore the drift is also perpendicular to the magnetic field [1].

As mentioned in the introduction, an $\boldsymbol{E} \times \boldsymbol{B}$-drift arises due to charge separation that is caused by the ∇B-drift discussed above. The $\boldsymbol{E} \times \boldsymbol{B}$-drift arises when plasma particles are following the electric field lines. Due to their velocity they are deflected by the Lorentz force. At a certain point this deflection makes them move against the electric field. This slows them down, by which the influence of the Lorentz force decreases. This process repeats and as a result an $\boldsymbol{E} \times \boldsymbol{B}$-drift arises as visualized in Figure 2.2.

These described guiding center drifts lead to particles moving outwards in a fusion reactor [1]. Particle confinement is therefore one of the challenges of fusion research.

Another effect caused by a nonuniform magnetic field is the existence of magnetic mirrors, which play a role in the W7-X configurations High and Low Mirror. Here, the magnetic field strength varies in space along the magnetic field direction. This can lead to particles getting trapped between regions where the magnetic field is particularly strong. The principle behind the trapping is the conservation of magnetic moment and the conservation of energy of the particle.
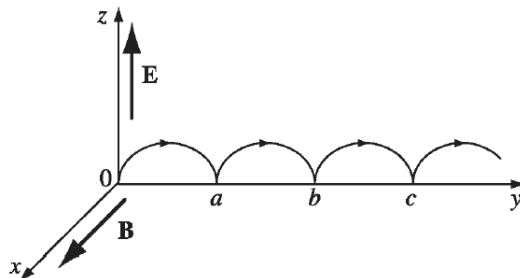

Figure 2.2: Visualization of the $\boldsymbol{E} \times \boldsymbol{B}$-drift [12].

The magnetic moment is defined as

$$\mu = \frac{1}{2} m_a v_\perp^2 / B. \tag{2.1}$$

In order to conserve magnetic moment, $v_\perp$ must increase when B increases. In order to conserve energy, consequently $v_\parallel$ must decrease. When B is large enough that $v_\parallel$ goes to zero, the particle is reflected by the high-B-region, like a mirror. In this way, particles can get trapped in this so called magnetic mirror [1].

In order to describe or simulate the behaviour of particles in a plasma, various equations are used. Solving these equations is hard due to the high amount of dimensions needed to describe the dynamics. To simplify this number of dimensions, gyrokinetic theory is used. This is discussed in the next section.

Gyrokinetic theory

To describe the behaviour of plasma particles, continuity equations and equations for the conservation of energy and momentum are needed. Kinetic theory uses a particle distribution function $f(\boldsymbol{r}, \boldsymbol{v}, t)$ to describe the particle's motion [1]. This function is thus dependent on seven variables. It needs to satisfy the fundamental Boltzmann equation

$$\frac{\partial f}{\partial t} + \boldsymbol{v} \cdot \nabla f + \frac{\boldsymbol{F}}{m} \cdot \frac{\partial f}{\partial \boldsymbol{v}} = \left(\frac{\partial f}{\partial t} \right)_c, \tag{2.2}$$

where $\mathbf{F}$ is the net force acting on the particle, and $\left(\frac{\partial f}{\partial t} \right)_c$ denotes the rate of change of f in time due to collisions. To get a complete set of equations describing the particles' dynamics, also the quasi-neutrality condition

$$n_e \approx n_i \approx n \tag{2.3}$$

is necessary. Here, n_e is the electron density, n_i is the ion density and n is the plasma density.

This set of equations is six dimensional and is therefore incredibly hard to solve. Gyrokinetic theory cuts down the number of dimensions needed by one, since it averages out the θ-dependence. This simplifies the equations and cuts down on computational costs when solving these equations with simulations. Leaving the θ-dependence out of the equations is done by approximating the gyromotion of a particle as a circle moving in space. This is visualized in Figure 2.3. To account for the motion of the particle in θ-direction, this motion is averaged by taking the integral over this motion and dividing it by 2π. To account for the motion in space, the average is taken, resulting in the motion of the guiding center. This is represented by the continuous line on the right hand side of Figure 2.3. With these approximations, the set of equations becomes 5-dimensional in stead of 6-dimensional. This makes it a little easier to simulate turbulence, although it is still expensive to solve these 5D equations. Simulating turbulence is discussed after the next section, in which the ion temperature gradient instability will be discussed.
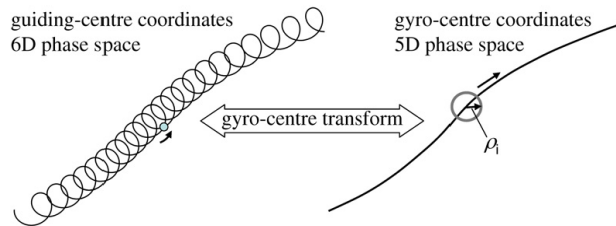

Figure 2.3: Less coordinates are needed to describe the particle's motion in gyrokinetic theory when the θ-dependence is averaged out [10].

2.2 Ion temperature gradient instability

As explained in the introduction, instabilities arise when perturbations grow. The ion temperature gradient arises therefore since there are perturbations in temperature present in the plasma. Ions move due to the ∇B-drift and due to the differences in velocity of hotter or colder ions, they create areas where the ion density is higher or lower. This leads to a potential difference between these areas. Due to this potential difference and the electric field that arises from it, an $\boldsymbol{E} \times \boldsymbol{B}$ flow arises. This $\boldsymbol{E} \times \boldsymbol{B}$ flow lets the ion temperature gradient increase even more since colder ions are flowing towards hotter ones and hotter ones are flowing towards colder ones [3]. This growing perturbation leads to instability. An evolution of this ion temperature gradient instability is shown in Figure 2.4.
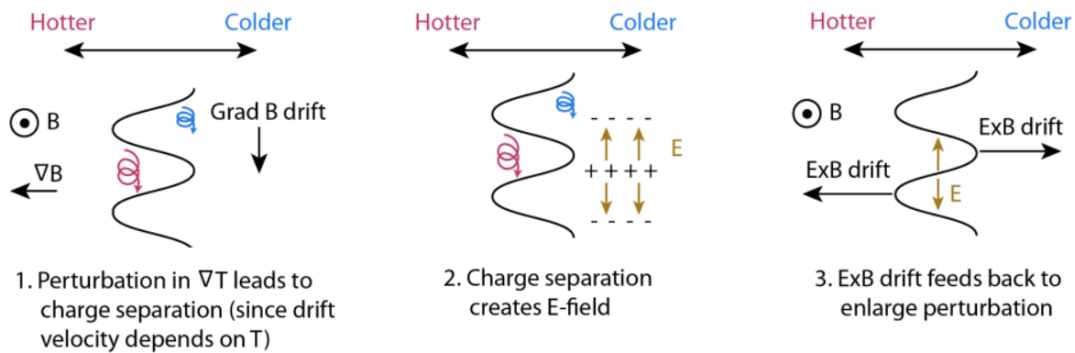

Figure 2.4: Evolution of the ITG instability. Adapted from [24].

2.3 Simulating and modelling turbulence

In chapter 3, the simulation data that are used for the research described in this report will be discussed. In the present section, the way turbulence is simulated is explained to give an image of how this data is retrieved.

To solve the gyrokinetic equations, the GENE code [15] is used, which simulates in a flux-tube domain with periodic boundaries. A flux tube is a small volume around a specific magnetic field line, followed around the whole torus. The GENE code simulates full turbulence in Fourier space. In spatial coordinates a flux tube can be described using r, θ and z, where r is the radial coordinate, θ is the poloidal coordinate and z is the coordinate in the direction of the magnetic field line. In Fourier space these coordinates are k_x, k_y and k_z respectively [25]. k_x and k_y are the radial and poloidal wave number. The radial and poloidal dimensions of the flux tube are then

$$L_x = \frac{2\pi}{k_x}, L_y = \frac{2\pi}{k_y}. \tag{2.4}$$

The wave numbers are the inverse of the dimensions of the eddies. This means that when a bigger flux tube is used in the simulations, bigger eddies, representing stronger turbulence, are taken into account.

As explained in the introduction, to improve energy confinement in fusion reactors, it is desired to predict the heat flux

$$Q = -\chi \nabla T, \tag{2.5}$$

where χ is the heat conductivity. This can be done using a model to predict χ using linear simulations. For this model, relations between nonlinear and linear simulations need to be found to represent the strength of turbulence and zonal flows of nonlinear simulations using linear simulations only.

The output of simulations is a spectrum of the turbulence. For this research the electrostatic potential ϕ is simulated, which means the spectrum is a collection of all the amplitudes of the fluctuations of the electrostatic potential contributing to the turbulence and zonal flows.

Linear simulations

Using linear simulations, turbulence can be expressed as

$$\sum_{k_y} \frac{\gamma_{k_y}}{k_y \rho_{ti}}, \tag{2.6}$$

where γ is the growth rate of the ion temperature gradient and ρ_{ti} is the ion thermal radius as defined in equation 1.2. Using liner simulations, the linear zonal flow response is expressed as

$$\mathcal{R}_{k_x}(t) = \frac{\langle \phi_{k_x, k_y=0}(t) \rangle}{\langle \phi_{k_x, k_y=0}(0) \rangle}. \tag{2.7}$$

For the zonal flow response $k_y = 0$ since the zonal flows are constant in the poloidal direction. The linear zonal flow response consists of a fast gyro acoustic mode (GAM) oscillation at the beginning, where after it decays towards a residual value [26] [13] [10] [17] [23]. An example of the linear zonal flow response is shown in Figure 3.1 in the next chapter.

Nonlinear simulations

Using nonlinear simulations, the nonlinearly simulated turbulence is expressed as the squared turbulent potential fluctuation

$$\mathcal{T} = \frac{1}{2} \sum_{k_x, k_y \neq 0} \langle |\tilde{\phi}_{k_x, k_y}|^2 \rangle. \tag{2.8}$$

This is thus the sum over all k_x and k_y of all squared contributions of the fluctuations of the electrostatic potential, $\tilde{\phi}$. The angular brackets denote the average over the flux surface.

The nonlinear zonal flow contribution is expressed as

$$\mathcal{Z} = \frac{1}{2} \sum_{k_x} \langle |\tilde{\phi}_{k_x, k_y=0}|^2 \rangle. \tag{2.9}$$

Modelling turbulence

To retrieve information on turbulence in a cheaper way, $\mathcal{T}$ has been related to the linear turbulence. These linear turbulent spectra are often found well correlated to nonlinear spectra. For W7-X, this gives a linear relation shown in Figure 2.5.

There has not been established a general way to retrieve the zonal flow contribution in a cheaper way yet. In Nunamis model, one possible way is used, which worked for the LHD. He found a linear relation between $\sqrt{\frac{\mathcal{Z}}{\mathcal{T}}}$ and the zonal flow decay time

$$\tau_{ZF} = \int_0^{\tau_f} \mathcal{R}_{k_x}(t) dt, \tag{2.10}$$

which is the integral over the linear zonal flow response [6]. Here, τ_f is the time at which the residual value of the linear zonal flow response is reached. The zonal flow decay time is defined by Ferrando-Margalet, Sugama and Watanabe in their paper *Zonal flows and ion temperature gradient instabilities in multiple-helicity magnetic fields* [6]. The relation found for Nunami's model is shown in Figure 2.6.
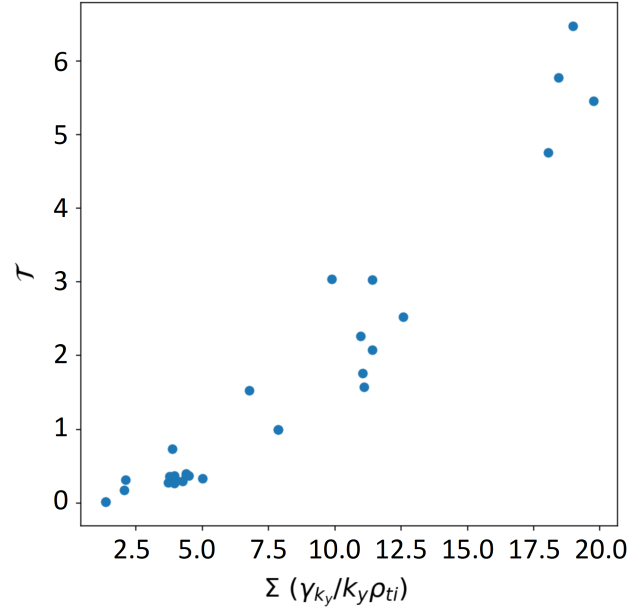
Figure 2.5: Linear relation found between linear and nonlinear simulations of turbulence for W7-X. Figure made by C.D. Mora Moreno, 2019.

In Nunami's model, $\tau_f = 25R_0/v_{ti}$ is used for the upper limit of the zonal flow decay time. Here, R_0 is the major radius and v_{ti} is the ion thermal velocity. It is argued in their paper that the zonal flow response function does not influence the zonal flow level for times greater than $25R_0/v_{ti}$ since the correlation time is smaller [19]. However, in Ferrando-Margalet's paper, τ_f is defined as the time at which the residual value of the linear zonal flow response is reached [6].

A linear relation between $\sqrt{\mathcal{Z}/\mathcal{T}}$ and τ_{ZF} is not found for W7-X as well. Thus, a different characteristic of the linear zonal flow response needs to be found that represents the strength of the zonal flow response and is related to the nonlinear zonal flow reponse strength. Therefore the research discussed in this report aims at investigating the relation between linear and nonlinear zonal flow response for W7-X. The methods used for this research are discussed in the next chapter.
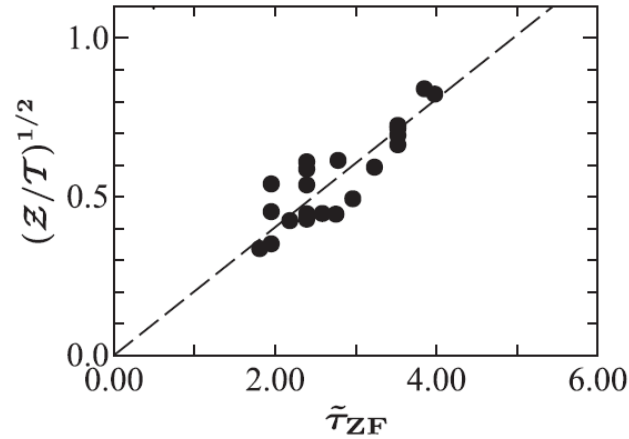

Figure 2.6: $\sqrt{\mathcal{Z}/\mathcal{T}}$ against the zonal flow decay time τ_{ZF} for the LHD [19].

Chapter 3

Research description

This chapter describes the methods of the performed research. First, the data that is used is discussed. Second, processing the data to characterize the linear zonal flow potential is discussed. Third, the methods used to quantify the characteristics of the linear zonal flow response are discussed. Finally, the method used to find relations between these characteristics and the nonlinear zonal flow strength is discussed. In Chapter 4, the results from this research are presented.

3.1   Linear data

The GENE code [15] was used to simulate the electrostatic potential ϕ, following the gyrokinetic approach, as explained in section 2.3. Our investigations were conducted in collisionless plasmas. This means that it is assumed that the temperature of the plasma particles is high enough that particles do not feel each others electrical field when they move past each other and therefore do not collide [2].

From the linear simulations, the real and imaginary parts of the linear zonal flow electrostatic potential as a function of time are retrieved. To take the effects of geometry into account, different W7-X configurations were investigated and the simulations were done at different normalized radii s as well. The configurations, Standard Configuration (sd), High Mirror (hm), Low Mirror (lm), High Iota (hi) and Low Iota (li), are discussed in the introduction. Furthermore, we investigated the zonal flow response using different widths of the flux tube, L_x, to investigate in which dimensions of the flux tube the physics is still captured correctly. In total, 42 data sets obtained with linear simulations are used. The specifications of each data set is given in table 3.1.

Note that a significant number of linear simulations were performed with $L_x = 104.719$. This provides a common ground to compare the linear zonal flow response amongst configurations and radii. This specific L_x is chosen since this L_x is related to the reference value $k_r \rho_i = 0.06$, explained in the paper *Zonal Flow Dynamics and Control of Turbulent Transport in Stellarators* by Xanthopoulos et al. as the wave number for which zonal flow oscillations emerge and are distinguishable from GAM oscillations [26].

3.2   Nonlinear data

As discussed in section 2.3, the nonlinear contributions of turbulence and zonal flow response are defined as the nonlinear zonal flow amplitude $\mathcal{T}$ and $\mathcal{Z}$. Using nonlinear simulations of the ITG instability, $\mathcal{Z}$ and $\mathcal{T}$ are retrieved. In total, 26 data sets obtained with nonlinear simulations are used. The parameters varied in the nonlinear simulations are shown in table 3.2. Again, different configurations, s and L_x values were used. Since turbulence levels rise proportionally to the ion temperature gradient, it is also relevant to investigate the zonal flow contribution at different

gradients. The ion temperature gradient in GENE is defined as

$$\omega_{Ti} \equiv a \left(\nabla T_i\right) / T_i, \tag{3.1}$$

where a is the minor radius of the device, ∇T is the gradient of the temperature and T_i is the temperature of species i [22]. Therefore also simulations with different ω_{Ti} values were performed.

Table 3.1: Specifications of the linear data sets

Number	Configuration	s	L_x	Number	Configuration	s	L_x
1	hi	0.5	104.719	22	lm	0.5	104.719
2	hi	0.5	110.997	23	lm	0.5	136.837
3	hi	0.5	665.979	24	lm	0.5	684.184
4	hi	0.8	104.719	25	lm	0.9	104.719
5	hm	0.36	104.719	26	sd	0.25	104.719
6	hm	0.36	530.418	27	sd	0.25	774.957
7	hm	0.5	104.719	28	sd	0.36	104.719
8	hm	0.5	310.957	29	sd	0.36	436.870
9	hm	0.5	621.914	30	sd	0.5	104.719
10	hm	0.8	78.832	31	sd	0.5	130.316
11	hm	0.8	104.719	32	sd	0.5	260.633
12	hm	0.8	266.000	33	sd	0.5	621.914
13	hm	0.8	530.000	34	sd	0.6	104.719
14	li	0.5	104.719	35	sd	0.6	138.185
15	li	0.5	340.925	36	sd	0.6	198.992
16	li	0.5	681.850	37	sd	0.8	68.805
17	li	0.6	104.719	38	sd	0.8	95.562
18	li	0.7	104.719	39	sd	0.8	104.719
19	li	0.8	90.837	40	sd	0.8	137.610
20	li	0.8	104.719	41	sd	0.9	59.952
21	li	0.9	104.719	42	sd	0.9	104.719

Table 3.2: Specifications of the nonlinear data sets

Configuration	s	L_x	ω_{Ti}	Configuration	s	L_x	ω_{Ti}
hi	0.5	665.979	1	sd	0.25	774.957	2
hi	0.5	110.997	1.3	sd	0.25	774.957	3
hi	0.5	110.997	1.5	sd	0.36	436.870	1
hm	0.5	310.957	1	sd	0.36	436.870	3
hm	0.5	310.957	2	sd	0.5	260.633	1
hm	0.5	310.957	3	sd	0.6	198.992	1
hm	0.8	78.832	2.3	sd	0.6	198.992	2
li	0.5	340.925	1	sd	0.6	138.185	2
li	0.5	681.85	1	sd	0.6	198.992	3
li	0.8	90.837	1.5	sd	0.8	68.805	1
lm	0.5	684.184	1	sd	0.8	68.805	2
lm	0.5	136.837	2	sd	0.8	137.610	1
sd	0.25	774.957	1	sd	0.9	59.952	1

3.3 Characterizing the linear zonal flow response

The first steps of the research were to characterize the behaviour of the linear zonal flow response. The real and imaginary parts and the modulus of the linear electrostatic potential, were compared to analyze their behaviour. All moduli, real parts and imaginary parts are normalized. We plotted the normalized modulus, real part and imaginary part as a function of time for all data sets. An example is shown in Figure 3.1, where the modulus, real part and imaginary part of the linear zonal flow response of Standard Configuration at normalized radius $s = 0.5$ in a flux tube with dimension $L_x = 104.719$ are plotted against time.
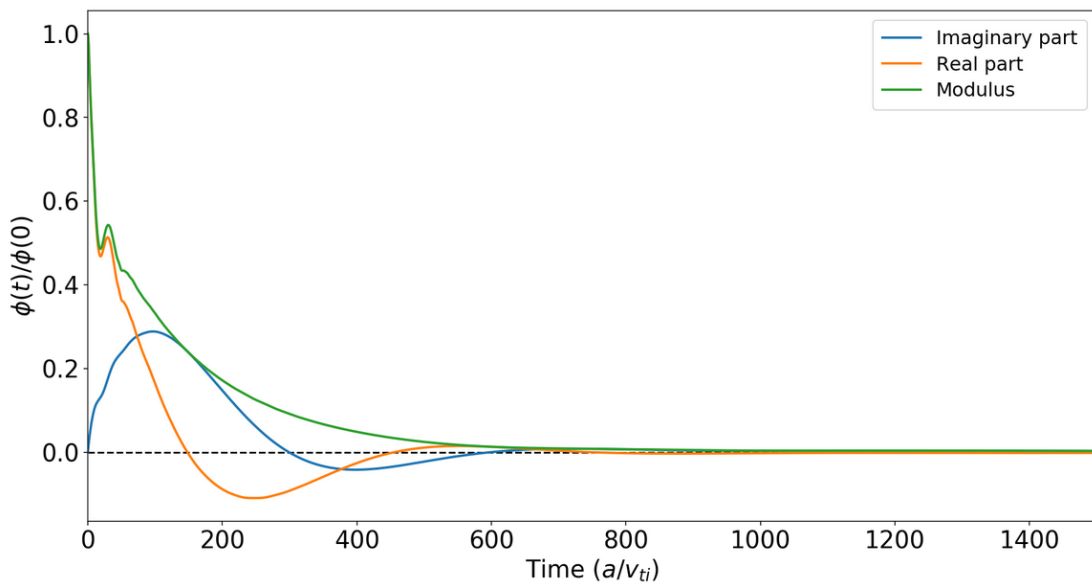

Figure 3.1: The modulus, real part and imaginary part of the linear zonal flow response of Standard Configuration at normalized radius $s = 0.5$ in a flux tube with dimension $L_x = 104.719$ plotted against time.

The linear zonal flow responses of all linear simulations are compared and patterns in its behaviour are observed. This is done to identify characteristics that can represent the zonal flow strength and can be related to the nonlinear zonal flow response, but as well to understand its behaviour better. Investigating the behaviour of the linear zonal flow response might also be useful for assembling models without needing to use linear simulations even, although this is not the purpose of our research. The results are discussed in section 4.1.

The methods used to quantify these characteristics are discussed in the next sections.

3.3.1 Residual value

The linear zonal flow response goes to a residual value after some time, as described in section 1.4. Zooming in on plots that were made of the linear zonal flow response, it shows clearly that the residual values change smoothly within very small values. The zonal flow response does not go to zero. A higher residual value means that there are more zonal flows still present in the plasma, suggesting that more turbulence is suppressed. We therefore would expect to see a positive correlation between the residual value and nonlinear zonal flow response.

Since these changes observed in the linear zonal flow response after some time are small, we approximate the residual as a constant value. To determine this value, the following method is used.

The derivative with respect to time of the linear zonal flow response is calculated at each point in time. When this derivative is significantly low and stays low, the zonal flow response does not

change much any more. The time frame in which the linear zonal flow response has its residual value, is quantified by setting a criterion on the derivative of the linear zonal flow response in this time frame. The following condition is used:

$$|(Q[n+1] - Q[n])/(t[n+1] - t[n])| < 0.00001.$$

Where Q[n] is the value of the modulus of the linear zonal flow response of index number n of the data set, and t[n] is the time corresponding to this Q. A second and third condition for this time frame is that the above condition needs to be satisfied for the whole time frame, and that the final point in time that is collected by the data needs to be part of it. In this way, it is ensured that points in time where the derivative is also very low, for instance at a minimum or maximum in the oscillations of the linear zonal flow response, are not mistaken for being points in time at which the residual value is reached. The critical value 0.00001 is chosen since using this critical value reproduces residual values in the right order of magnitude as expected by observing the plots.

Eventually, the residual value is calculated by taking the average over the values of Q in the whole time frame that is established with the above method. The error of the residual is determined by calculating the standard deviation of these values. The results from this are discussed in section 4.2. In Figure 3.2, an example is shown of the determined residual value plotted together with the linear zonal flow response. It shows that the calculated residual is in the right order of magnitude. This example is from Standard Configuration at normalized radius $s = 0.25$ in a flux tube with dimension $L_x = 774.957$.
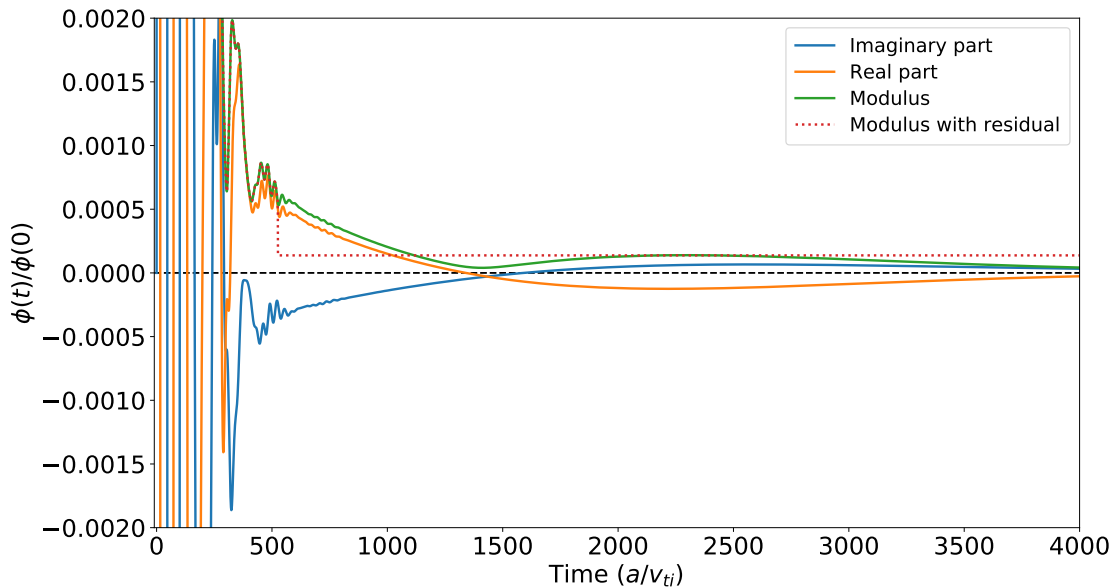

Figure 3.2: The calculated residual value is plotted together with the modulus, real part and imaginary part of the linear zonal flow response of Standard Configuration at normalized radius $s = 0.25$ in a flux tube with dimension $L_x = 774.957$.

3.3.2 Zonal flow decay time

The zonal flow decay time is discussed in section 2.3. We assume that when the zonal flow decay time is high, the zonal flow response decays slow and will suppress more turbulence. When it is low, the zonal flow response has decayed fast and less turbulence has been suppressed. We therefore would expect a positive correlation between the zonal flow decay time and nonlinear zonal flow response.

To calculate the zonal flow decay time for all linear data sets, the integral over the normalized modulus of the zonal flow response was taken. For τ_f, the first time at which the linear zonal flow response has reached its residual value is used. We thus used τ_f as defined in the definition of the zonal flow decay time, whereas for Nunami's model a different τ_f was used, as explained in section 2.3.

The same integrals over the imaginary and real parts of the linear zonal flow response up to the same τ_f are calculated as well, to analyse the contribution of each component.

The results from this are discussed in section 4.3.

3.3.3 Fitting of an exponentially damped cosine

The real part of the linear zonal flow response resembles an exponentially damped oscillator. To quantify the oscillation frequency a and the decay constant b, the function

$$y(t) = \cos(at)\exp(-bt)$$

is fitted on the normalized real part. Oscillations in the zonal flow response are related to how much the zonal flows shear the turbulent eddies, as described in *Oscillations of zonal flows in stellarators* by Helander et al [13]. We thus expect a higher oscillation frequency to be related to higher nonlinear zonal flow response. For the decay constants, we expect a higher decay constant to be related to a faster decay of zonal flows, and thus less suppression of turbulence. Therefore we expect a negative correlation between the decay constants and nonlinear zonal flow response. The results of the fit are discussed in section 4.4.

Having discussed now the methods used to quantify characteristics of the linear zonal flow response, the investigations done on finding a relation between these linear characteristics and the nonlinear zonal flow response are described in the next section.

3.4 Investigating the relation between linear and nonlinear zonal flow response

For the final steps of this research we compared the quantified characteristics of the linear zonal flow response to the nonlinear zonal flow contribution. Since zonal flows arise from turbulent oscillations, it is important to note that the nonlinear zonal flow strength is a function of $\mathcal{Z}$ and $\mathcal{T}$ [19];

$$\mathcal{F}(\mathcal{T}, \mathcal{Z}) = \frac{\mathcal{T}^n}{\mathcal{Z}^m}. \tag{3.2}$$

However, here the coefficients n and m of this function are heuristic. Two of the used coefficients, were extracted from the following publications: $\frac{\mathcal{T}}{\sqrt{\mathcal{Z}}}$ is used in the paper *Gyrokinetic turbulent transport simulation of a high ion temperature plasma in large helical device experiment* by Nunami et al. in reference [20] to approximate χ, and $\sqrt{\frac{\mathcal{Z}}{\mathcal{T}}}$ is used for establishing the linear relation between linear and nonlinear zonal flow response for the LHD in Nunami's model in reference [19].

Therefore, an heuristically approach is used choosing the following relations that we used to plot against the linear characteristics:

$$\sqrt{\frac{\mathcal{Z}}{\mathcal{T}}}, \sqrt{\frac{\mathcal{T}}{\mathcal{Z}}}, \frac{\mathcal{T}}{\sqrt{\mathcal{Z}}}, \frac{\sqrt{\mathcal{Z}}}{\mathcal{T}} \tag{3.3}$$

These particular functions of $\mathcal{Z}$ and $\mathcal{T}$ were chosen because they are comparable to the relation used for Nunami's model. However, it must be remembered that they are not fully supported by theory. In order to find a coefficient relating the linear and nonlinear zonal flow strength, scatter plots were made of the linear characteristics against these nonlinear relations.

First, these relations were plotted against the zonal flow decay time and the integral over the real part of the linear zonal flow response, to verify that the same relation as found for Nunami's model is not found for W7-X. From these plots, it is concluded that $\sqrt{\mathcal{Z}/\mathcal{T}}$ and $\sqrt{\mathcal{Z}}/\mathcal{T}$ are not adequate to use for investigating the relation between nonlinear and linear data, since they are negatively correlated to the linear zonal flows characteristics. Therefore, only $\mathcal{T}/\sqrt{\mathcal{Z}}$ and $\sqrt{\mathcal{T}/\mathcal{Z}}$ are plotted against the other characteristics. It is important to keep in mind that the nonlinear data is retrieved using different normalized radii s and different dimensions of the flux tube L_x, therefore no conclusions can be drawn of the found relations regarding the result at only one normalized radius s or the results retrieved using only one dimension for the flux tube L_x. The results are discussed in section 4.5.

Chapter 4

Results

Having discussed how the research is conducted in chapter 3, the results are presented in the present chapter. Conclusions drawn of these results are discussed in chapter 5.

4.1 Characterizing the linear zonal flow response

Using the linear simulation data, plots are made of the modulus, real part and imaginary part of the zonal flow response as a function of time. The section below describes general observations that are helpful to find characteristics that represent the linear zonal flow response strength, to understand its behaviour better and to provide a reference for comparing the observed behaviour to the results of the other parts of the research.

As an example, a plot of the simulation data from Standard Configuration at normalized radius $s = 0.6$ is shown in Figure 4.1.
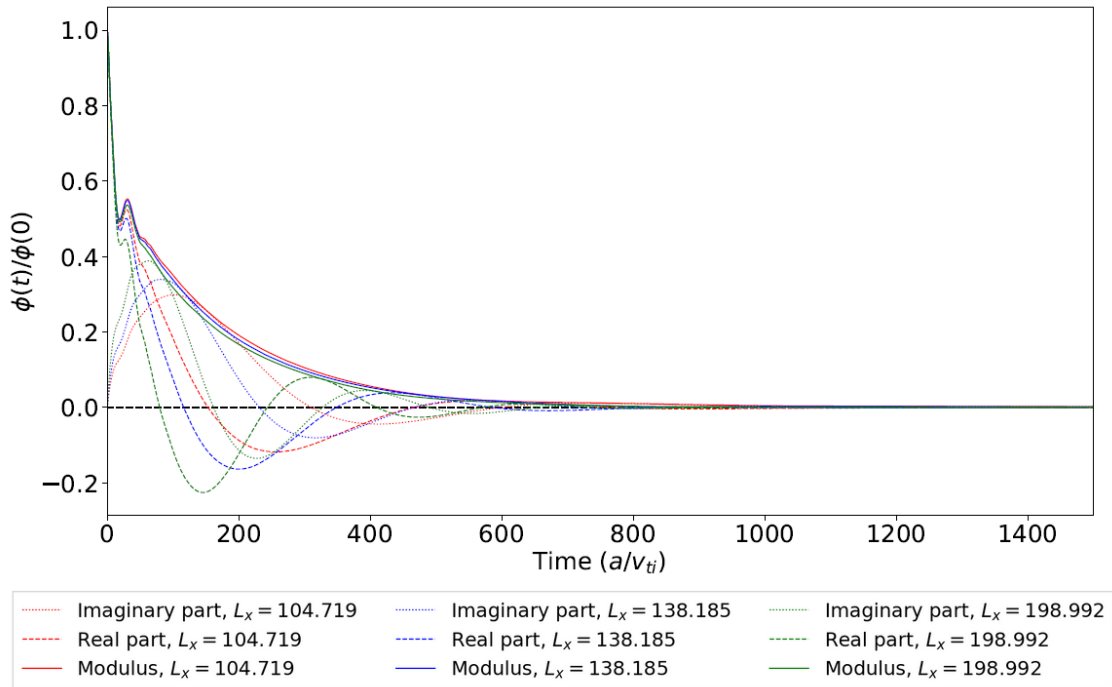
Figure 4.1: Linear zonal flow response for the Standard Configuration at normalized radius $s = 0.6$ for different dimensions of the flux tube L_x.

All plots show a linear zonal flow response that decays in time and that oscillates. Therefore, it is chosen to quantify the residual, the integral over the modulus, the integral over both the real part and imaginary part, the angular frequency of the oscillations, and the decay constant. These characteristics could possibly represent the zonal flow strength and can be related to the nonlinear zonal flow response.

Next, briefly the observations made when comparing the linear zonal flow response to identify the behaviour in different geometries and for different dimensions of the flux tubes are discussed.

The configurations were varied, while comparing data at one normalized radius s retrieved with a specific dimension of the flux tube L_x, it is observed that for different configurations, both oscillation frequency as well as the strength of the damping vary. The modulus of the linear zonal flow response is shown for all configurations at normalized radius $s = 0.5$ and in a flux tube with dimension $L_x = 104.719$ in Figure 4.2. In the beginning, the zonal flow response of High Iota decays the slowest, followed by High Mirror, Standard Configuration, Low Mirror and Low Iota. However, soon the zonal flow response of High and Low Mirror decay faster than the others and oscillations begin to show. The behaviour of the oscillations can be divided in two parts: in the beginning phase, it shows only one small bump, visible around $t = 50 a/v_{ti}$ on Figure 4.2. After this, the zonal flow response starts oscillating more after some time in which it only decays. The frequency and amplitude of these oscillations differs per configuration. The real and imaginary parts of the zonal flow response all oscillate. The modulus of configurations High and Low Mirror oscillate the most. The modulus of Standard Configuration does not show oscillations in most cases, and the modulus of High and Low Iota is slightly oscillating. From these observations combined of the decay and the oscillations, it is expected that the zonal flow activity in High Mirror and High Iota are the highest, since a slow decay and more oscillations are expected to be related to a high zonal flow activity as explained in chapter 3. They are followed by Low Mirror, the Standard Configuration and Low Iota.
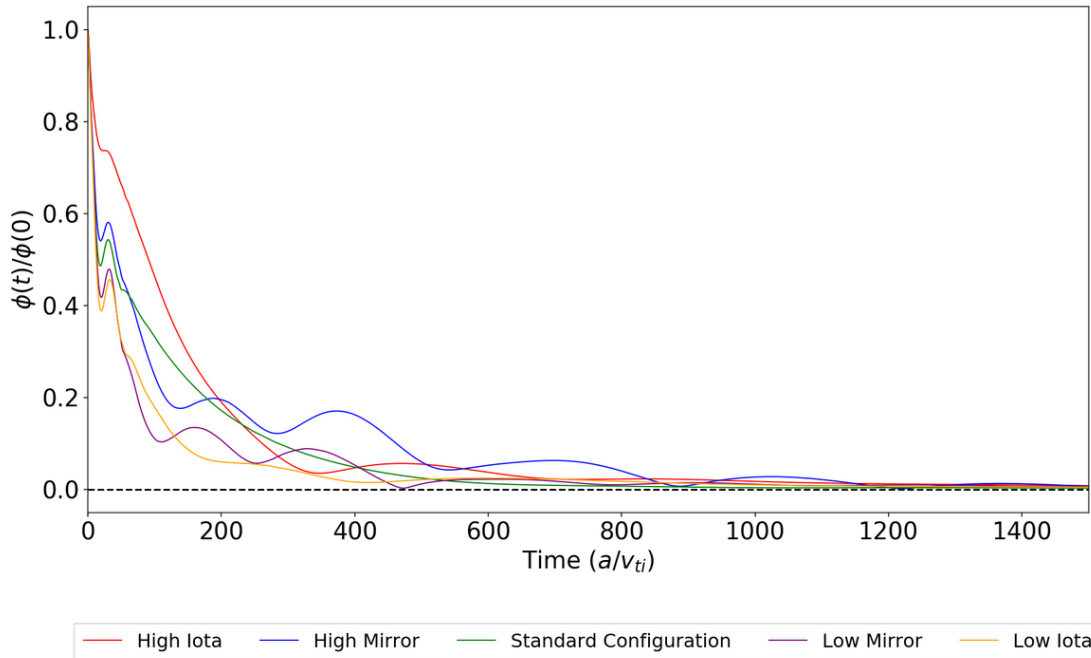

Figure 4.2: Linear zonal flow response for all configurations at $s = 0.5$ and with in a flux tube with dimension $L_x = 104.719$.

Varying the dimension of the flux tube L_x while comparing data from one configuration at one normalized radius s, it is observed that when L_x increases, the modulus, real part and imaginary part decay faster and the amplitude of the oscillations is higher. The example in Figure 4.1 shows

that this is the case. When L_x is bigger, more bands of zonal flows are simulated. A possible explanation for the faster decay is that when two bands next to each other flow in opposite directions, these contributions cancel each other. A possible explanation for the bigger amplitude of the oscillations is that when more bands are present, the direction of the flows differs more, causing thus bigger oscillations.

Varying the normalized radius s while comparing data from one configuration using one dimension of the flux tube L_x, it is observed that the behaviour at different s can be separated in two: the behaviour for low s values, for our simulations between $s = 0.25$ and $s = 0.6$, and for high s values, for our simulations between $s = 0.7$ and $s = 0.9$. This behaviour is clearly visible in the case of the imaginary parts of the linear zonal flow response for the Standard Configuration in a flux tube with dimension $L_x = 104.719$, shown in Figure 4.3. For the small s values, it holds in general that when s gets bigger, the imaginary and real part grow more, and their decay is slower. For the big s values, it holds in general that when s gets bigger, the imaginary and real part grow less, and have a lower maximum or minimum. The linear zonal flow response depends clearly on the location in the plasma, and it is particularly different towards the edge of the plasma.

The behaviour of the modulus of the linear zonal flow response is not different for low and big s. It decays in general slower at bigger s. Thus, there are more zonal flows present at big s, which, intuitively, makes sense because at the edge there is more turbulence present due to the higher temperature gradients, so more zonal flows are generated and more turbulence is present to be suppressed, leading to a longer lifetime of the zonal flows. However, these are linear simulations in which no turbulence is simulated, since turbulence is a nonlinear effect. So it is remarkable to see that in the linear simulations, which are evolutions of initial perturbation given in the computational domain, reproduce this intuitively correct behaviour. However, if we compare this behaviour to figure 1.5 in the introduction that shows that the global magnetic shear varies in different regions, this behaviour of the linear zonal flow response is not in line with this. Figure 1.5 show that more global magnetic shear is present at high s, which means that less turbulence is present. The figure showed that at bigger normalized radius s, the magnetic shear is higher. Therefore, we would expect that the zonal flow response is lower at bigger s, since there is less turbulence present to generate the zonal flows.
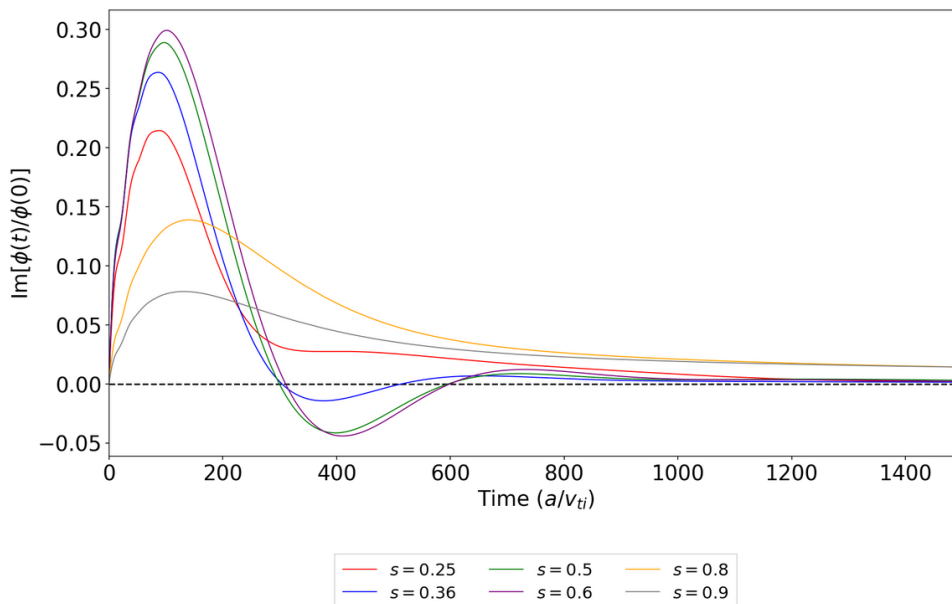

Figure 4.3: Imaginary parts of the linear zonal flow response for the Standard Configuration with in a flux tube with dimension $L_x = 104.719$, at different s.

4.2 Residual value

The residual values of all data found by the method described in section 3.3.1 are shown in Figure 4.4. The residual values and their errors are also written down in table A.1 in the appendix. Some results are somewhat counter intuitive. For instance the values differ in order of magnitude, ranging from 10^{-5} - 10^{-2}. Furthermore, it can be seen that in general, the residual value for any configuration at a certain normalized radius s seems to be lower when the dimension of the flux tube L_x is higher. A possible explanation for this might be that using a bigger flux tube means that more zonal flows are present, averaging out each others strength when moving in opposite directions, and therefore giving a lower residual value. Relatively high values of the residual are found at bigger normalized radius s, which is as expected since higher zonal flows are expected at the edge of the plasma. However, not all residual values at big radius s are high, so it seems that L_x plays a role in the value of the residual as well.
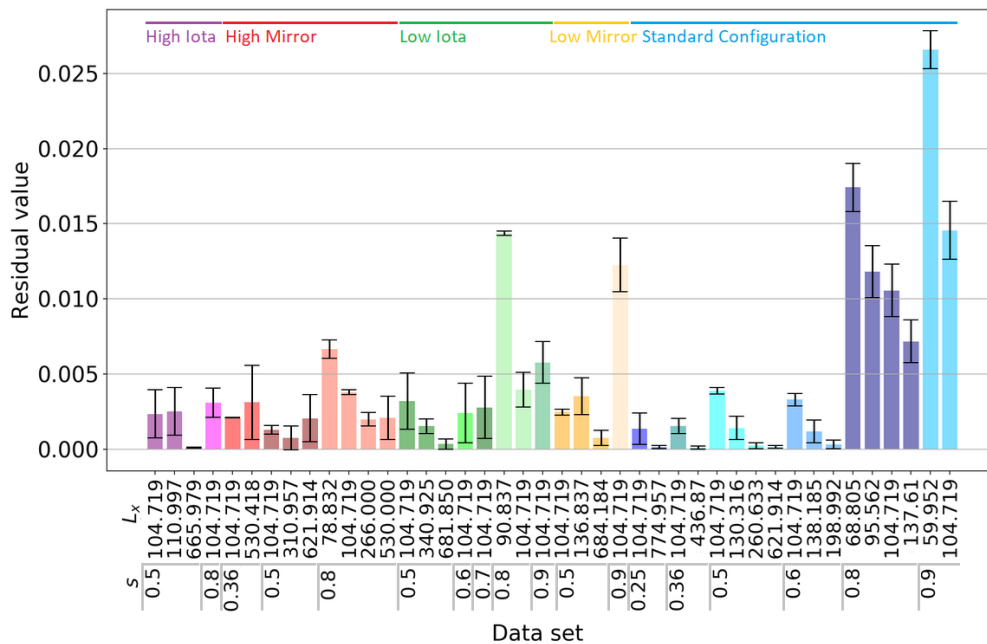
Figure 4.4: Residual values for each data set.

Figure A.1 in the appendix shows the residual values for all simulations done in a flux tube with dimension $L_x = 104.719$. This figure reveals that for High Mirror and Low Iota, as we go away from the plasma core, a decrease in the residual values is observed, until $s = 0.6$ is reached: then the residual value increases when moving even further away from the plasma core towards the edge. This behaviour cannot be explained. For Standard Configuration, the residual increases in general for each s when we go away from the plasma core. For High Iota and Low Mirror the residual increases for bigger s values but no conclusion can be drawn on the behaviour for low s values, since there is no data retrieved in this region. An increasing residual when moving outwards in the plasma makes sense, because there would be more turbulence present at the edge of the plasma.

4.3 Zonal flow decay time

The zonal flow decay times of all linear simulations were obtained by the method described in section 3.3.2 and are shown in Figure 4.5.
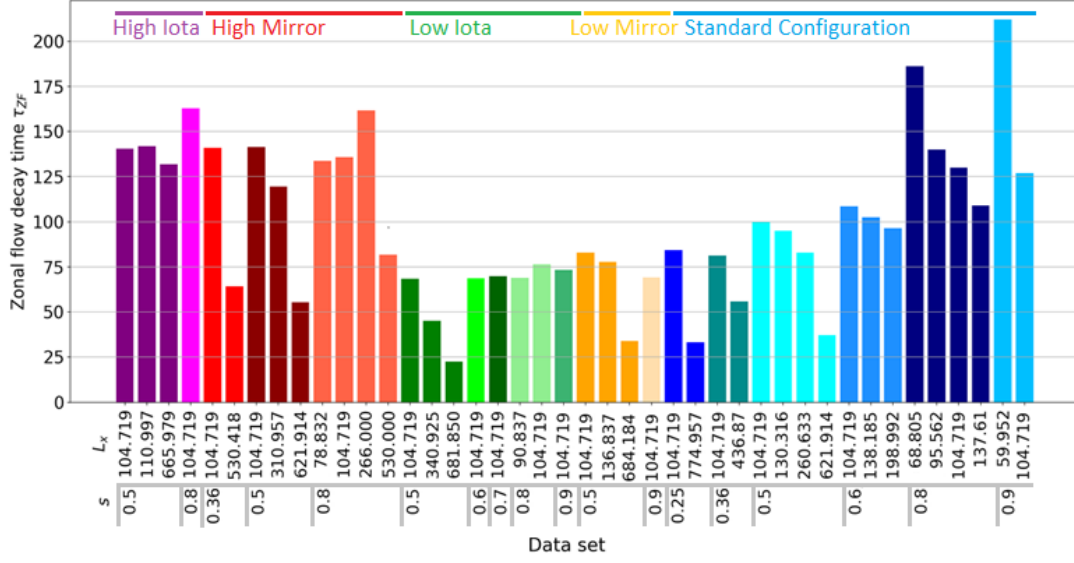
Figure 4.5: Zonal flow decay time for each data set.

As described in chapter 3, the integral over the real parts of the linear zonal flow response are obtained as well and they are shown in Figure 4.6. The calculated integral over the imaginary parts are shown in Figure A.2 in the appendix.
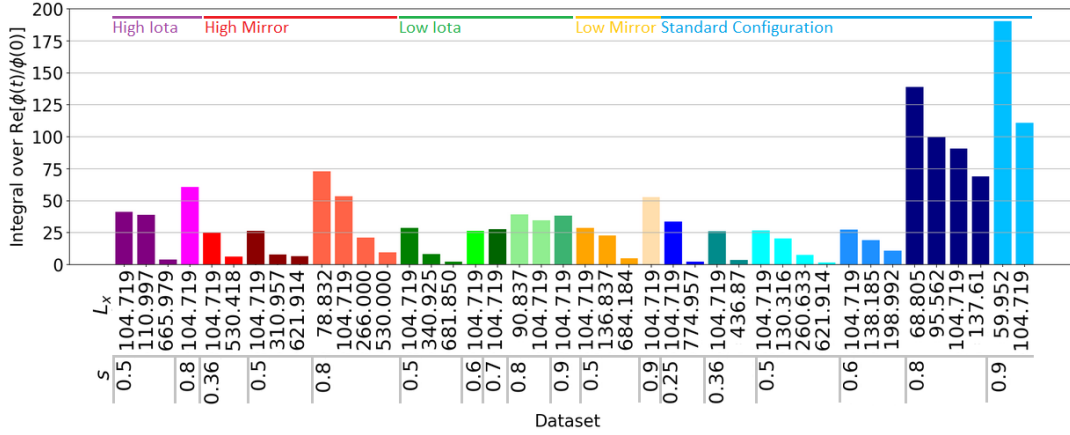

Figure 4.6: Integral over $\text{Re}[\phi(t)/\phi(0)]$ for each data set.

Figure 4.5 shows that in general, for any configuration at a certain normalized radius s, the zonal flow decay time gets lower when the dimension of the flux tube L_x gets bigger. As is shown in Figure 4.6, the integral over the real part always gets smaller when L_x gets bigger. In section 4.1 is found that a higher L_x is associated with a faster decay. It is likely that a faster decay means that the residual value is reached sooner and thus that the zonal flow decay time or the integral over the real part is smaller. So these results are in line with each other.

In figures A.3 and A.4 in the appendix, the zonal flow decay times and the calculated integrals over the real part of the linear zonal flow response for all simulations done in a flux tube with dimension $L_x = 104.719$ are shown. For Standard Configuration, High Iota and low Iota, a bigger s is related to a bigger zonal flow decay time. This is in line with the relation found in section 4.1 that a bigger s is related to a slower decay of the modulus of the zonal flow response. The zonal flow decay time for High Mirror and Low Mirror seems to be slightly lower for big s. A possible

explanation is that the oscillating behaviour of the zonal flow response in High and Low Mirror configurations causes the total integral to decrease.

From the relations found in section 4.1, it would be expected that for the low normalized radius s, in our case from $s = 0.25$ till $s = 0.6$, a bigger s is related to a higher integral over the real part of the zonal flow response. This is not observed in Figure A.4. It would be expected that for bigger s, in our case from $s = 0.7$ till $s = 0.9$, a bigger s is related to a less growing real and imaginary part, so a smaller value for the integral over $\text{Re}[\phi(t)/\phi(0)]$. This relation is also not observed in A.4.

4.4 Fitting of an exponentially damped cosine

The function $y(t) = \cos{(at)} \exp{(-bt)}$ is fitted on the real part of the linear zonal flow response. The method described in section 3.3.3 is limited in giving accurate results. In Figure 4.7 it can be seen how the equation is fitted on the normalized real part of the linear zonal flow response for High Iota at $s = 0.5$ with in a flux tube with dimension $L_x = 665.979$, as an example. Here, the fitting function has worked quite accurately. In Figure 4.8 however, it can be seen that the fitting function for High Mirror at $s = 0.36$ in a flux tube with dimension $L_x = 104.719$ has not worked very well. The fit is decent for the decay constant b but not for the angular frequency a.
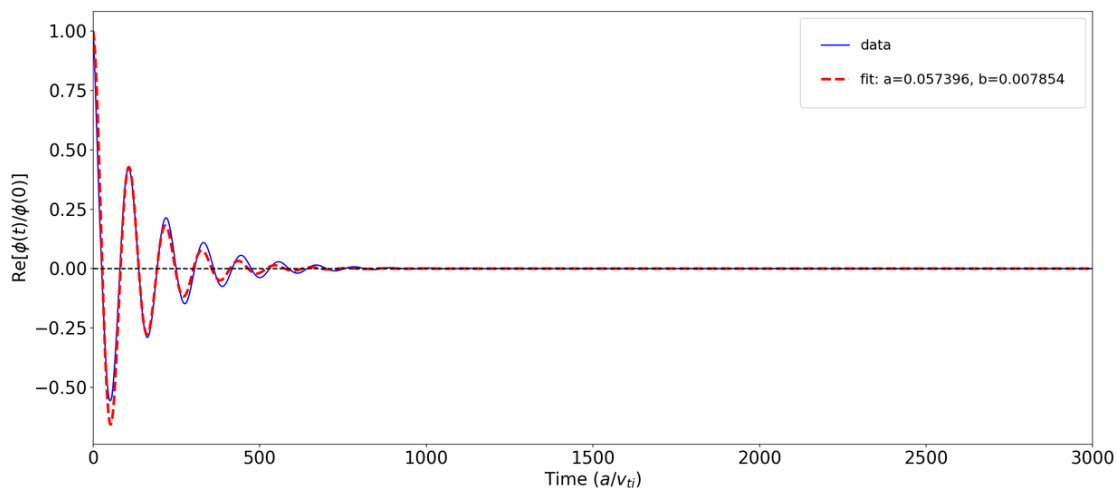

Figure 4.7: The normalized real part of the linear zonal flow response for High Iota at $s = 0.5$ with in a flux tube with dimension $L_x = 665.979$ where the fit provides parameters $a = 0.057396$ and $b = 0.007854$.

The angular frequencies a and decay constants b determined by the fits are shown in figures A.5 in the appendix and Figure 4.9 below. The fit for High Mirror at normalized radius $s = 0.5$ in a flux tube with dimension $L_x = 310.957$ (dataset 8) returned way higher values than all others, and is therefore left out. It is an unexpected result that the fitting routine is not quite accurate for the angular frequency of the High Mirror data, while the linear zonal flow response is the most oscillating for this configuration.

Figure A.5 in the appendix shows that the angular frequencies range from small values, that can not be seen on the figure, to larger values. There is also no clear relation between the configurations, or s and L_x values. Therefore, these results are no further analysed.

Figure 4.9 shows that the decay constants of High Iota are the lowest, followed by High Mirror, Standard Configuration, Low Mirror and Low Iota. This is consistent with the results shown in Figure 4.2. Taking only the data in a flux tube with dimension $L_x = 104.719$ into account, it shows that, in general, for each configuration the decay constant gets lower when s gets bigger. However this does not hold for the data sets with $s = 0.6$ and $s = 0.9$ of Low Iota. This is shown in
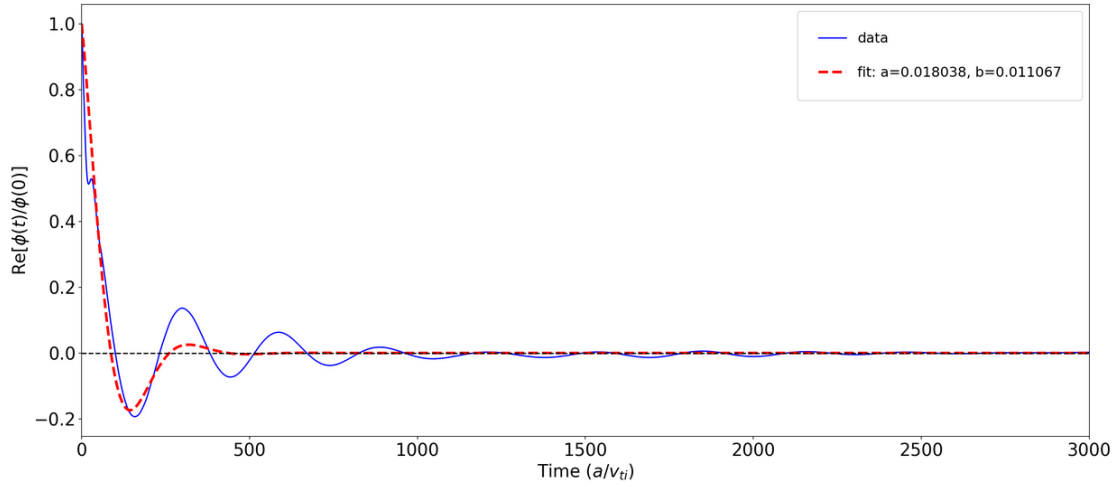
Figure 4.8: The normalized real part of the linear zonal flow response for High Mirror at $s = 0.36$ with in a flux tube with dimension $L_x = 104.719$ where the fit provides parameters $a = 0.018038$ and $b = 0.011067$.

Figure A.6 in the appendix. Figure 4.9 shows in addition that when taking one configuration and one specific normalized radius s into account, there is no clear relation between the dimension of the flux tube L_x and the decay constant. However it shows that high decay constants are related to big L_x values. This is in line with the results found in section 4.1 that a big L_x is linked to faster decay.
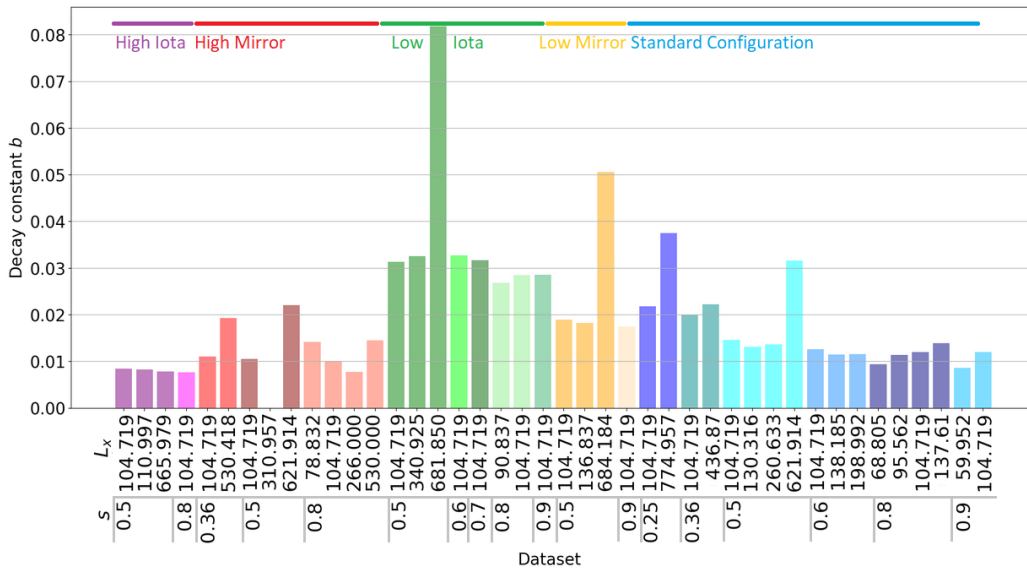
Figure 4.9: Decay constants b for each data set. The decay constant of High Mirror at normalized radius $s = 0.5$ in a flux tube with dimension $L_x = 310.957$ (dataset 8) is left out.

4.5 Investigating the relation between linear and nonlinear zonal flow response

Having quantified the characteristics of the linear zonal flow response, the relation between linear and nonlinear zonal flow response is investigated. The residual values, zonal flow decay times, integrals over the real parts of the linear zonal flow response and the decay constants are plotted against the functions of $\mathcal{Z}$ and $\mathcal{T}$ as discussed in 3.4.

Zonal flow decay time versus the nonlinear zonal flow response

First, scatter plots were made of $\sqrt{\mathcal{T}/\mathcal{Z}}$, $\mathcal{T}/\sqrt{\mathcal{Z}}$, $\sqrt{\mathcal{Z}/\mathcal{T}}$ and $\sqrt{\mathcal{Z}}/\mathcal{T}$ against the zonal flow decay time.

The plot of $\sqrt{\mathcal{Z}/\mathcal{T}}$ against the zonal flow decay time is shown in Figure 4.10. The marker style refers to the ω_{Ti} value. This figure shows clearly that the linear relation between $\sqrt{\mathcal{Z}/\mathcal{T}}$ and the zonal flow decay time found in Nunami's paper for the LHD cannot be found for W7-X as well.

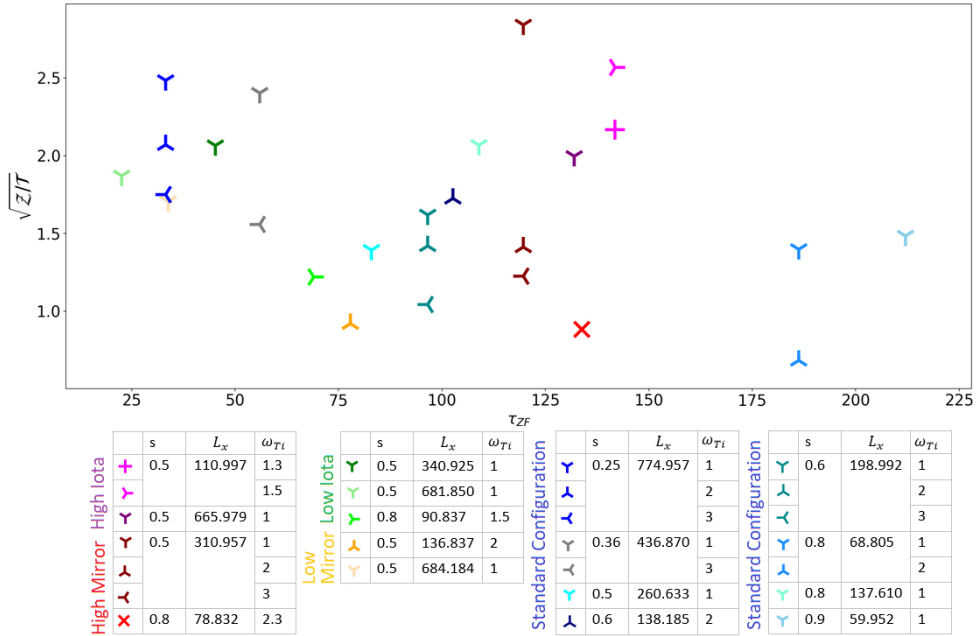|		s	L_x	ω_{Ti}			s	L_x	ω_{Ti}			s	L_x	ω_{Ti}			s	L_x	ω_{Ti}
High Iota	+	0.5	110.997	1.3	Low Iota	Y	0.5	340.925	1	Standard Configuration	Y	0.25	774.957	1	Standard Configuration	Y	0.6	198.992	1
	⊁			1.5		Y	0.5	681.850	1		⅄			2		⅄			2
	Y	0.5	665.979	1		⊱	0.8	90.837	1.5		⊰			3		⊰			3
High Mirror	Y	0.5	310.957	1	Low Mirror	⅄	0.5	136.837	2		Y	0.36	436.870	1		Y	0.8	68.805	1
	⅄			2		Y	0.5	684.184	1		⊰			3		⅄			2
	⊰			3							Y	0.5	260.633	1		Y	0.8	137.610	1
	✕	0.8	78.832	2.3							⅄	0.6	138.185	2		Y	0.9	59.952	1

Figure 4.10: $\sqrt{\mathcal{Z}/\mathcal{T}}$ plotted against the zonal flow decay time.

From the four plots as mentioned above that were made it is concluded that $\sqrt{\mathcal{Z}/\mathcal{T}}$ and $\sqrt{\mathcal{Z}}/\mathcal{T}$ are not adequate to find a relation between linear and nonlinear zonal flow response, since they are negatively correlated to the zonal flow decay time.

Consequently, only the results from the scatter plots of $\sqrt{\mathcal{T}/\mathcal{Z}}$ and $\mathcal{T}/\sqrt{\mathcal{Z}}$ against the zonal flow decay time are shown in figures 4.11 and 4.12. The data shown here are from simulations with $\omega_{Ti} = 1$, since the most simulations were performed with this value. Only data with this value of ω_{Ti} is shown here because in that way less variables used for the simulations in which the data is retrieved are taken into account.

Integral over the real part of the linear zonal flow response versus the nonlinear zonal flow response

To check whether for a different linear characteristic $\sqrt{\mathcal{Z}/\mathcal{T}}$ and $\sqrt{\mathcal{Z}}/\mathcal{T}$ are not adequate as well, scatter plots were made of $\sqrt{\mathcal{T}/\mathcal{Z}}$, $\mathcal{T}/\sqrt{\mathcal{Z}}$, $\sqrt{\mathcal{Z}/\mathcal{T}}$ and $\sqrt{\mathcal{Z}}/\mathcal{T}$ against the integral over the
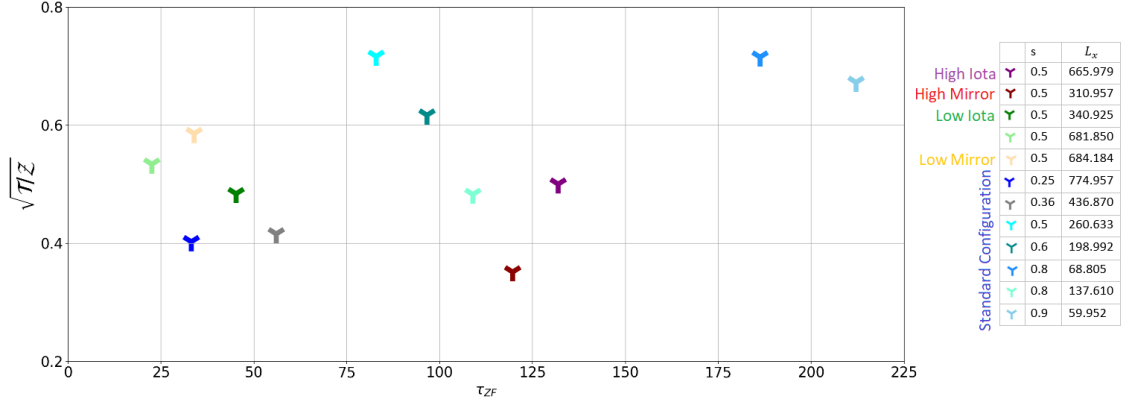
Figure 4.11: Scatter plot of $\sqrt{\mathcal{T}/\mathcal{Z}}$ against τ_{ZF}. This plot only shows the data with $\omega_{Ti} = 1$.
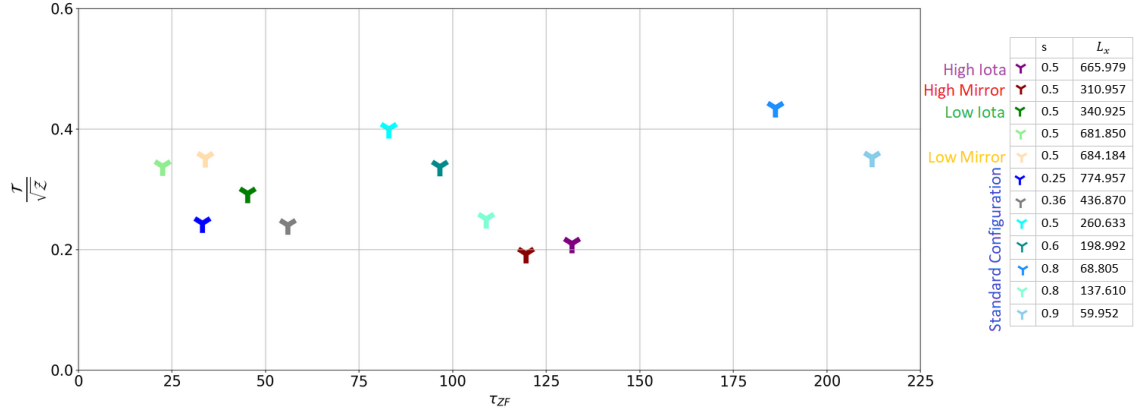

Figure 4.12: Scatter plot of $\mathcal{T}/\sqrt{\mathcal{Z}}$ against τ_{ZF}. This plot only shows the data with $\omega_{Ti} = 1$.

normalized real part of the linear zonal flow response. Again, the scatter plots of $\sqrt{\mathcal{Z}/\mathcal{T}}$ and $\sqrt{\mathcal{Z}}/\mathcal{T}$ against the integral over the real part showed a negative correlation. Consequently, only the results from the scatter plots of $\sqrt{\mathcal{T}/\mathcal{Z}}$ and $\mathcal{T}/\sqrt{\mathcal{Z}}$ against the integral over the real part of the linear zonal flow response are shown in figures 4.13 and 4.14.

Figures 4.11, 4.12, 4.13 and 4.14 show that there cannot be established a relation between $\sqrt{\mathcal{T}/\mathcal{Z}}$ or $\mathcal{T}/\sqrt{\mathcal{Z}}$ and the zonal flow decay time or the integral over $\text{Re}[\phi(t)/\phi(0)]$ based on this data.

Residual value versus the nonlinear zonal flow response

The residual values are plotted against $\sqrt{\mathcal{T}/\mathcal{Z}}$ and $\mathcal{T}/\sqrt{\mathcal{Z}}$. The results are shown in Figure 4.15 and 4.16. These figures shows clearly that there is no relation between the residual value and $\sqrt{\mathcal{T}/\mathcal{Z}}$ or $\mathcal{T}/\sqrt{\mathcal{Z}}$.

Since in these figures data with different ω_{Ti} values are taken into account, these figures show that for a higher ω_{Ti}, the nonlinear contribution is higher. This is expected since a higher temperature gradient is related to more turbulence.

Decay constants versus the nonlinear zonal flow response

The decay constants are plotted against $\sqrt{\mathcal{T}/\mathcal{Z}}$ and $\mathcal{T}/\sqrt{\mathcal{Z}}$. The results are shown in figures 4.17 and 4.18. Again, the decay constant of the data set of High Mirror at normalized radius $s = 0.5$ in a flux tube with dimension $L_x = 310.957$ is not taken into account. The figures show
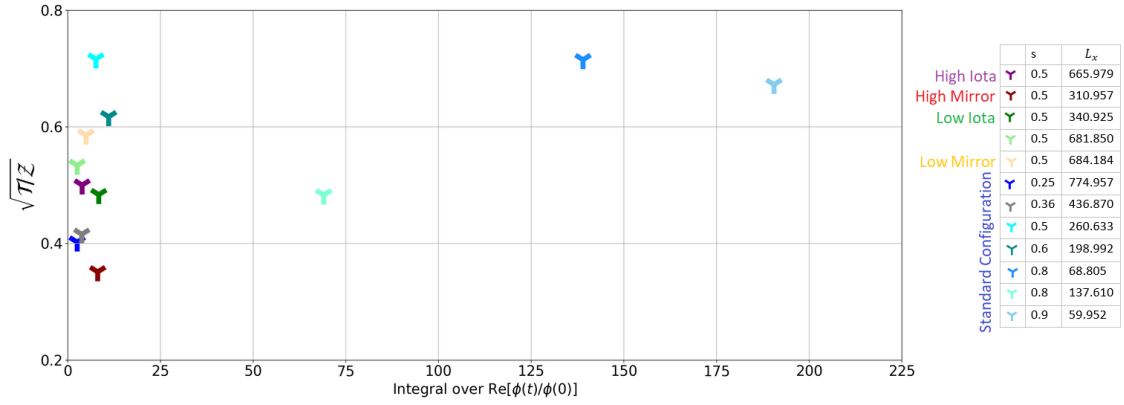
		s	L_x
High Iota	Y	0.5	665.979
High Mirror	Y	0.5	310.957
Low Iota	Y	0.5	340.925
	Y	0.5	681.850
Low Mirror	Y	0.5	684.184
	Y	0.25	774.957
	Y	0.36	436.870
	Y	0.5	260.633
	Y	0.6	198.992
	Y	0.8	68.805
	Y	0.8	137.610
	Y	0.9	59.952

Figure 4.13: Scatter plot of $\sqrt{\mathcal{T}/\mathcal{Z}}$ against the integral over $\mathrm{Re}[\phi(t)/\phi(0)]$ until the residual is reached. This plot only shows the data with $\omega_{Ti} = 1$.

		s	L_x
High Iota	Y	0.5	665.979
High Mirror	Y	0.5	310.957
Low Iota	Y	0.5	340.925
	Y	0.5	681.850
Low Mirror	Y	0.5	684.184
	Y	0.25	774.957
	Y	0.36	436.870
	Y	0.5	260.633
	Y	0.6	198.992
	Y	0.8	68.805
	Y	0.8	137.610
	Y	0.9	59.952
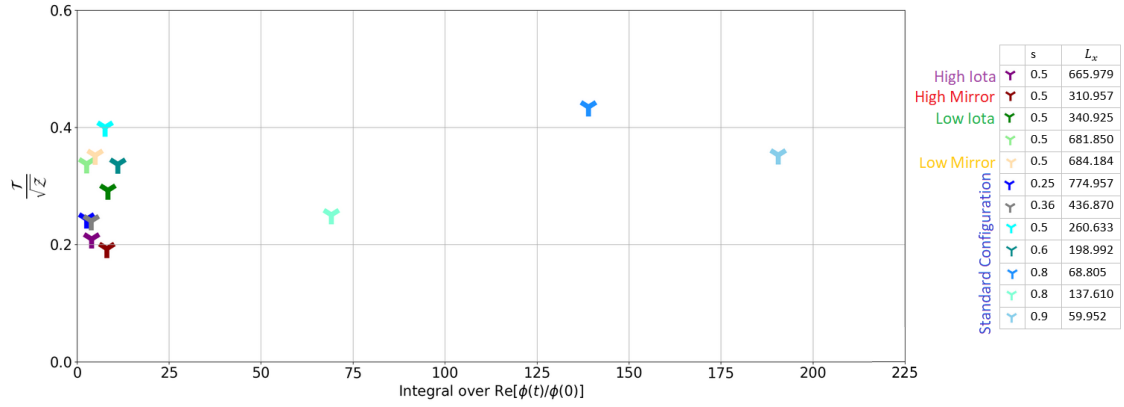
Figure 4.14: Scatter plot of $\mathcal{T}/\sqrt{\mathcal{Z}}$ against the integral over $\mathrm{Re}[\phi(t)/\phi(0)]$ until the residual is reached. This plot only shows the data with $\omega_{Ti} = 1$.

no relation between the decay constants and $\sqrt{\mathcal{T}/\mathcal{Z}}$ or $\mathcal{T}/\sqrt{\mathcal{Z}}$. Although when looking at only the data retrieved for Standard Configuration, since the most data is from this configuration, it looks like the data points are not positioned entirely random. However, the data points are from data with varying s and L_x and this makes it hard to draw conclusions since there is thus variety in the method or retrieving the data. Therefore it is not possible to really observe a trend.
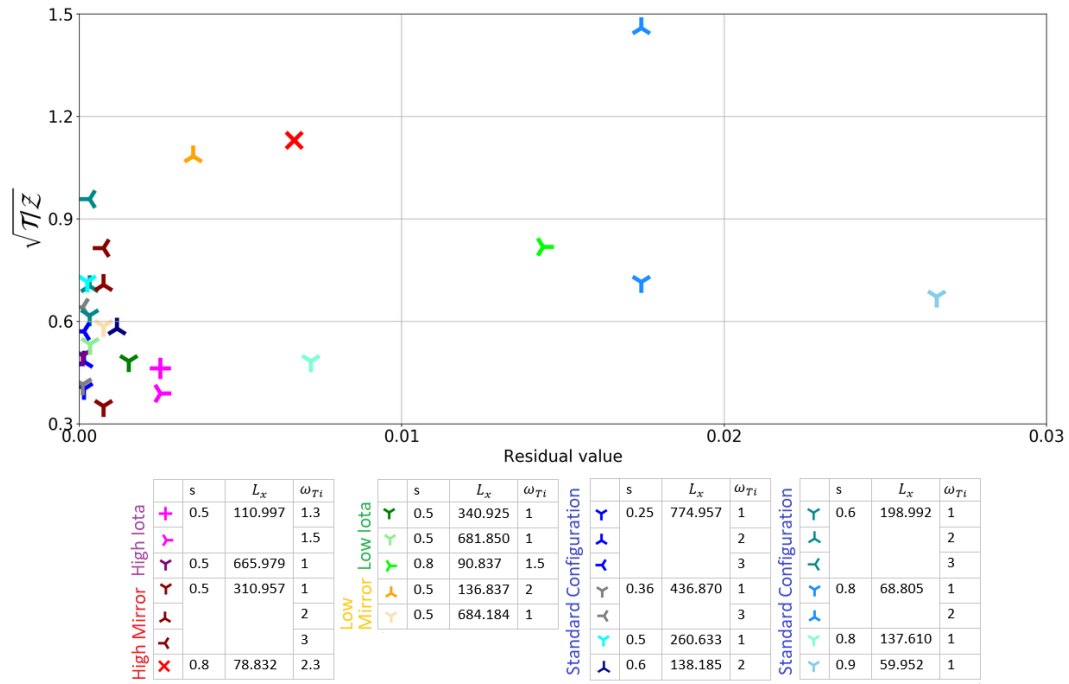
Figure 4.15: Scatter plot of $\sqrt{\mathcal{T}/\mathcal{Z}}$ against the residual value.
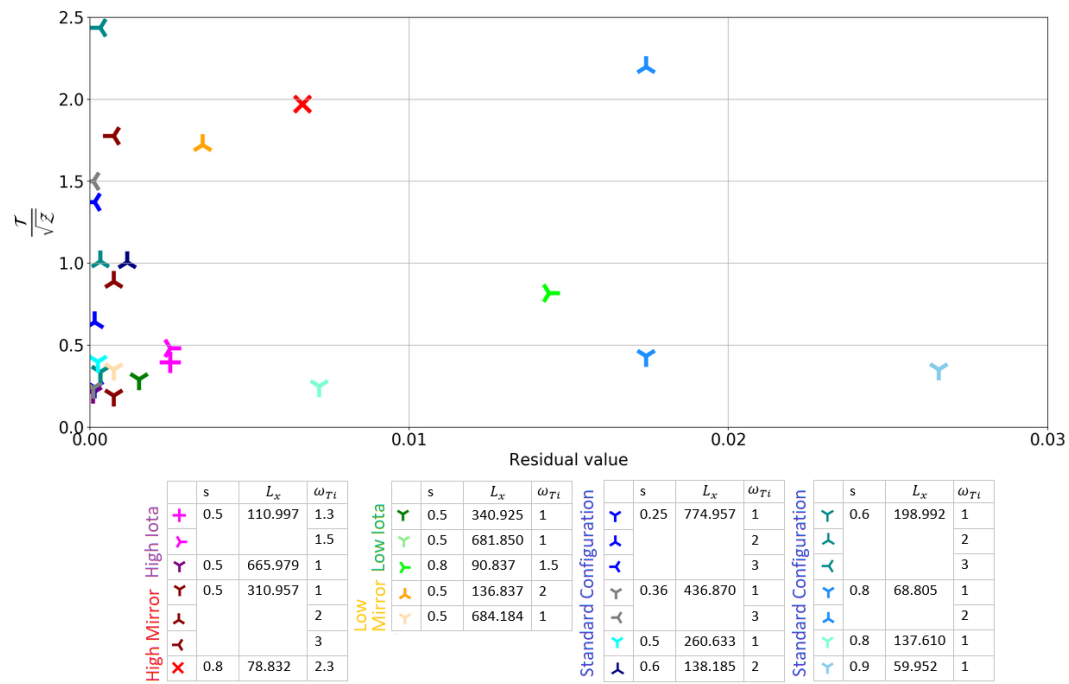
		s	L_x	ω_{Ti}		s	L_x	ω_{Ti}		s	L_x	ω_{Ti}		s	L_x	ω_{Ti}
High Iota	+	0.5	110.997	1.3	Y	0.5	340.925	1	Y	0.25	774.957	1	Y	0.6	198.992	1
	⋟			1.5	Y	0.5	681.850	1	⊥			2	⊥			2
	Y	0.5	665.979	1	⊱	0.8	90.837	1.5	◄			3	◄			3
High Mirror	Y	0.5	310.957	1	⊥	0.5	136.837	2	Y	0.36	436.870	1	Y	0.8	68.805	1
	⊥			2	Y	0.5	684.184	1	◄			3	⊥			2
	◄			3					Y	0.5	260.633	1	Y	0.8	137.610	1
	×	0.8	78.832	2.3					⊥	0.6	138.185	2	Y	0.9	59.952	1

Figure 4.16: Scatter plot of $\mathcal{T}/\sqrt{\mathcal{Z}}$ against the residual value.

		s	L_x	ω_{Ti}		s	L_x	ω_{Ti}		s	L_x	ω_{Ti}		s	L_x	ω_{Ti}
High Iota	+	0.5	110.997	1.3	Y	0.5	340.925	1	Y	0.25	774.957	1	Y	0.6	198.992	1
	⋟			1.5	Y	0.5	681.850	1	⊥			2	⊥			2
	Y	0.5	665.979	1	⊱	0.8	90.837	1.5	◄			3	◄			3
High Mirror	Y	0.5	310.957	1	⊥	0.5	136.837	2	Y	0.36	436.870	1	Y	0.8	68.805	1
	⊥			2	Y	0.5	684.184	1	◄			3	⊥			2
	◄			3					Y	0.5	260.633	1	Y	0.8	137.610	1
	×	0.8	78.832	2.3					⊥	0.6	138.185	2	Y	0.9	59.952	1
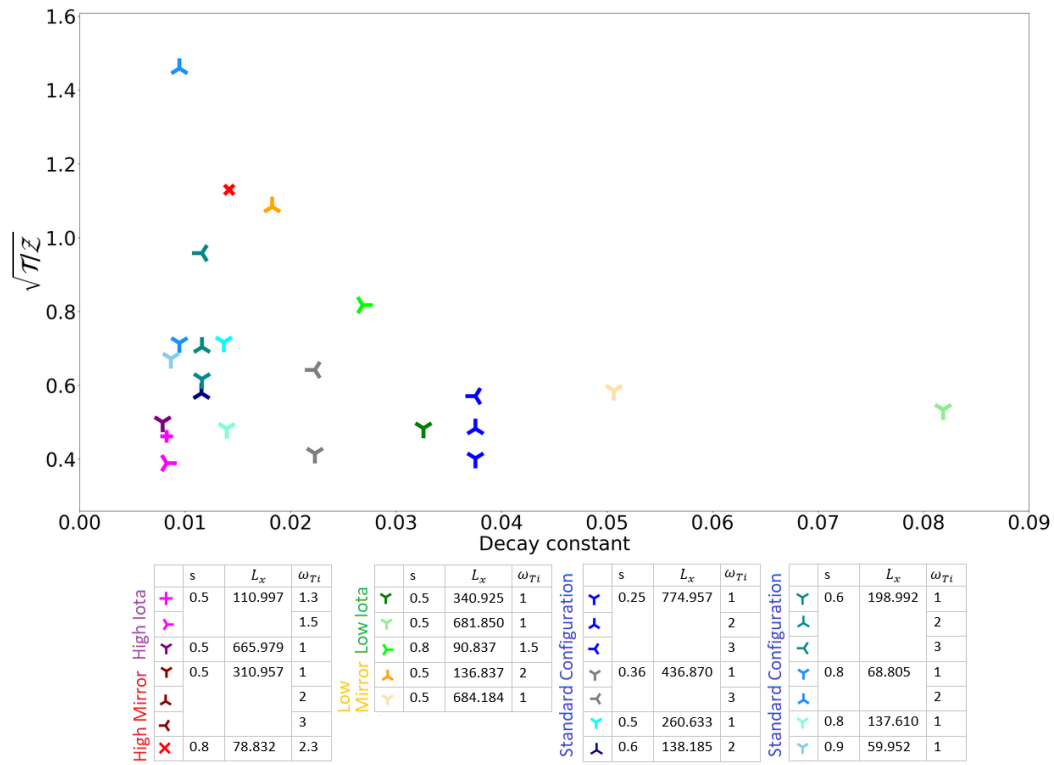
Figure 4.17: Scatter plot of $\sqrt{\mathcal{T}/\mathcal{Z}}$ against the decay constants.

High Mirror / High Iota

	s	L_x	ω_{Ti}
+	0.5	110.997	1.3
➤			1.5
Y	0.5	665.979	1
Y	0.5	310.957	1
⅄			2
◄			3
✗	0.8	78.832	2.3

Low Mirror / Low Iota

	s	L_x	ω_{Ti}
Y	0.5	340.925	1
Y	0.5	681.850	1
➤	0.8	90.837	1.5
⅄	0.5	136.837	2
Y	0.5	684.184	1

Standard Configuration

	s	L_x	ω_{Ti}
Y	0.25	774.957	1
⅄			2
◄			3
Y	0.36	436.870	1
◄			3
Y	0.5	260.633	1
⅄	0.6	138.185	2

Standard Configuration

	s	L_x	ω_{Ti}
Y	0.6	198.992	1
⅄			2
◄			3
Y	0.8	68.805	1
⅄			2
Y	0.8	137.610	1
Y	0.9	59.952	1
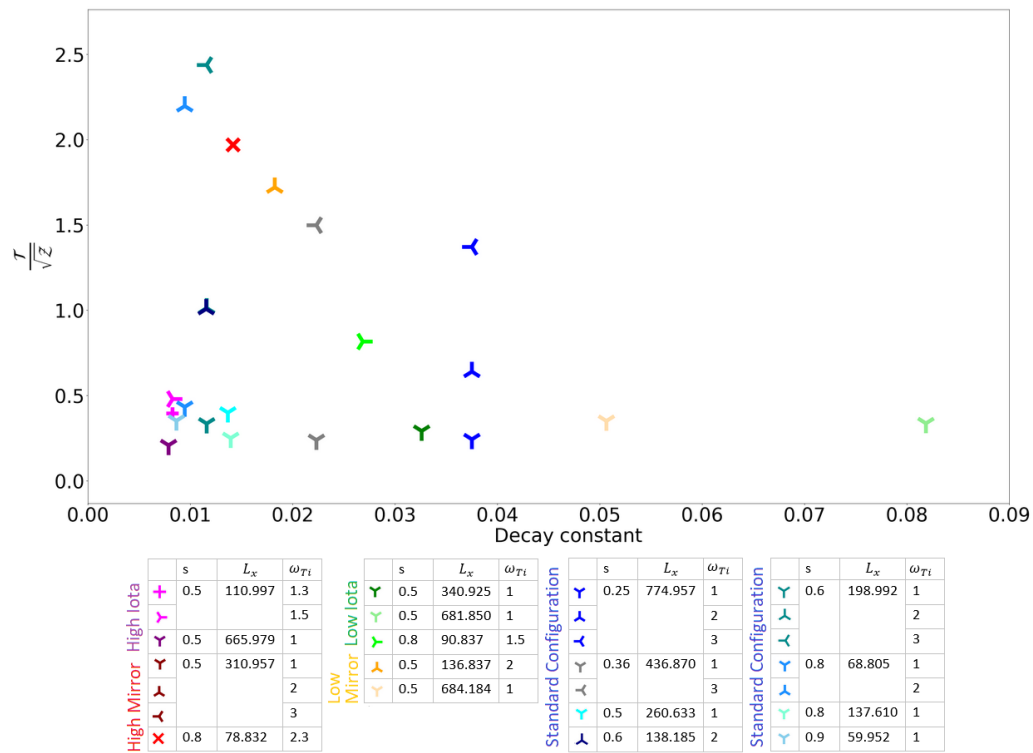
Figure 4.18: Scatter plot of $\mathcal{T}/\sqrt{\mathcal{Z}}$ against the decay constants.

High Mirror / High Iota

	s	L_x	ω_{Ti}
+	0.5	110.997	1.3
➤			1.5
Y	0.5	665.979	1
Y	0.5	310.957	1
⅄			2
◄			3
✗	0.8	78.832	2.3

Low Mirror / Low Iota

	s	L_x	ω_{Ti}
Y	0.5	340.925	1
Y	0.5	681.850	1
➤	0.8	90.837	1.5
⅄	0.5	136.837	2
Y	0.5	684.184	1

Standard Configuration

	s	L_x	ω_{Ti}
Y	0.25	774.957	1
⅄			2
◄			3
Y	0.36	436.870	1
◄			3
Y	0.5	260.633	1
⅄	0.6	138.185	2

Standard Configuration

	s	L_x	ω_{Ti}
Y	0.6	198.992	1
⅄			2
◄			3
Y	0.8	68.805	1
⅄			2
Y	0.8	137.610	1
Y	0.9	59.952	1

Chapter 5

Conclusion

To complete the application of the model described in section 2.3 for W7-X, we investigated the relation between linear and nonlinear zonal flow response. With a set of characteristics of the linear zonal flow response identified, it was attempted to find a contribution of the linear zonal flow response representative for the nonlinear zonal flow strength to incorporate in the model. The residual value, zonal flow decay time, integral over the real and imaginary parts of the zonal flow response, angular frequency and decay constants were quantified for the available linear data. This linear data was plotted against functions of the nonlinear zonal flow amplitude $\mathcal{Z}$ and the nonlinear turbulence fluctuations $\mathcal{T}$. Since plotting $\sqrt{\mathcal{Z}/\mathcal{T}}$ and $\sqrt{\mathcal{Z}}/\mathcal{T}$ against linear characteristics of the zonal flow response showed a negative correlation, it is concluded that they are not adequate to establish a relation between linear and nonlinear zonal flow response. Therefore, we can conclude that the linear relation between $\sqrt{\mathcal{Z}/\mathcal{T}}$ and the zonal flow decay time found in Nunami's model for the Large Helical Device cannot be found for W7-X as well. Furthermore, the zonal flow decay time is not a proper characteristic of the linear zonal flow response in W7-X, to be representative of the strength of the linear zonal flow contribution that can be related to the nonlinear one.

The relation between $\sqrt{\mathcal{T}/\mathcal{Z}}$ and $\mathcal{T}/\sqrt{\mathcal{Z}}$ and the quantified linear characteristics show no clear trend between linear and nonlinear zonal flow response.

The overall conclusion is that no relation could be established between the linear and nonlinear zonal flow response, and that the identified characteristics of the linear zonal flow response but also the functions of $\mathcal{Z}$ and $\mathcal{T}$ that were used are not adequate to complete a reduced model for the linear and nonlinear zonal flow response in Wendelstein 7-X.

Future research aimed at finding a relation between the linear and nonlinear zonal flow response in W7-X could try to quantify the frequency of the zonal flow oscillations to verify whether that can be the right characteristic to represent nonlinear zonal flow strength. Also, through the linear data plotted against nonlinear data a function could be fitted to determine for which coefficients of the function $\frac{\mathcal{T}^n}{\mathcal{Z}^m}$ the relation is linear.

List of Figures

List of Tables

Bibliography

[1] F.F. Chen. *Introduction to Plasma Physics and Controlled Fusion, Volume 1: Plasma Physics*. Springer, 2006. 9, 10, 11, 35

[2] F.F. Chen. *An Indispensable Truth, How Fusion Power Can Save the Planet*. Springer, 2011. 1, 2, 3, 15, 35

[3] S. C. Cowley, R. M. Kulsrud, and R. Sudan. Considerations of ion-temperature-gradient-driven turbulence. *Physics of Fluids B: Plasma Physics*, 3(10):2767–2782, 1991. 12

[4] P. H. Diamond, S.-I. Itoh, K. Itoh, and T. S. Hahm. Zonal flows in plasma — a review. *Plasma Physics and Controlled Fusion*, 47(5):R35–R161, apr 2005. 5, 6, 35

[5] R.A. Dunlap. *An Introduction to the Physics of Nuclei and Particles*, chapter 13 Fusion reactions, pages 175–196. Brooks/Cole Cengage Learning, 2004. 2, 4

[6] S. Ferrando-Margalet, H. Sugama, and T.-H. Watanabe. Zonal flows and ion temperature gradient instabilities in multiple-helicity magnetic fields. *Physics of Plasmas*, 14(12):122505, 2007. 13, 14

[7] O. Février. *Global modelling of magnetic island control in tokamaks*. PhD thesis, Aix-Marseille University, 2016. 3, 35

[8] J.P. Freidberg. *Ideal MHD*, chapter 7 Equilibrium: three-dimensional configurations, pages 223–326. Cambridge University Press, 2014. 4

[9] Max-Planck-Institut für Plasmaphysik. Fusion basics nuclear fusion status and prospects, 2019. 4, 35

[10] X. Garbet, Y. Idomura, L. Villard, and T.-H. Watanabe. Gyrokinetic simulations of turbulent transport. *Nuclear Fusion*, 50(4):043002, 2010. 5, 6, 11, 13, 35

[11] J. Geiger, C. D. Beidler, Y. Feng, H. Maaßberg, N. B. Marushchenko, and Y. Turkin. Physics in the magnetic configuration space of w7-x. *Plasma Physics and Controlled Fusion*, 57(1):014004, 2014. 4

[12] D.J. Griffiths. *Introduction to Electrodynamics*, chapter 5 Magnetostatics, pages 210–265. Pearson Education, Inc., 2013. 10, 35

[13] P. Helander, A. Mishchenko, R. Kleiber, and P. Xanthopoulos. Oscillations of zonal flows in stellarators. *Plasma Physics and Controlled Fusion*, 53(5):054006, apr 2011. 13, 19

[14] K. Itoh, S.-I. Itoh, P. H. Diamond, T. S. Hahm, A. Fujisawa, G. R. Tynan, M. Yagi, and Y. Nagashima. Physics of zonal flows. *Physics of Plasmas*, 13(5):055502, 2006. 6

[15] F. Jenko, W. Dorland, M. Kotschenreuther, and B. Rogers. Electron temperature gradient driven turbulence. *Physics of Plasmas*, 7:1904–1910, 2000. 12, 15

[16] Z. Lin, T. S. Hahm, W. W. Lee, W. M. Tang, and R. B. White. Turbulent Transport Reduction by Zonal Flows: Massively Parallel Simulations. *Science*, 281(5384):1835–1837, 1998. 6

[17] P. Monreal, I. Calvo, E. Sánchez, F. I. Parra, A. Bustos, A. Könies, R. Kleiber, and T. Görler. Residual zonal flows in tokamaks and stellarators at arbitrary wavelengths. *Plasma Physics and Controlled Fusion*, 58(4):045018, feb 2016. 13

[18] F.T.M. Nieuwstadt, B.J. Boersma, and J. Westerweel. *Turbulence — Introduction to Theory and Applications of Turbulent Flows*. Springer, 2016. 5

[19] M. Nunami, T.-H. Watanabe, and H. Sugama. A reduced model for ion temperature gradient turbulent transport in helical plasmas. *Physics of Plasmas*, 20(9):092307, 2013. iiiiii, 6, 14, 19, 35

[20] M. Nunami, T.-H. Watanabe, H. Sugama, and K. Tanaka. Gyrokinetic turbulent transport simulation of a high ion temperature plasma in large helical device experiment. *Physics of Plasmas*, 19(4):042504, 2012. 19

[21] J. Ongena and Y. Ogawa. Nuclear fusion: Status report and future prospects. *Energy Policy*, 96:770 – 778, 2016. 2

[22] M. J. Pueschel, B. J. Faber, J. Citrin, C. C. Hegna, P. W. Terry, and D. R. Hatch. Stellarator Turbulence: Subdominant Eigenmodes and Quasilinear Modeling. *Phys. Rev. Lett.*, 116(8):085001, Feb 2016. 4, 5, 16

[23] M. N. Rosenbluth and F. L. Hinton. Poloidal Flow Driven by Ion-Temperature-Gradient Turbulence in Tokamaks. *Phys. Rev. Lett.*, 80(4):724–727, 1998. 13

[24] A. Scheinberg. A graphic explanation of the ion temperature gradient (itg) instability, 2016. 12, 35

[25] M. Schneller. *Gyrokinetic Turbulence Simulations for ASDEX Upgrade Plasmas: Diffusivity of Beam Ions and Nitrogen Seeding Modificated Transport*, Masterthesis, Ulm University, 2009. 12

[26] P. Xanthopoulos, A. Mischchenko, P. Helander, H. Sugama, and T.-H. Watanabe. Zonal Flow Dynamics and Control of Turbulent Transport in Stellarators. *Phys. Rev. Lett.*, 107(24):245002, Dec 2011. 13, 15

Appendix A

Extra figures

Residual value

In table A.1 the residual values with errors for all linear data sets are given.

In figure A.1, the residual values of all data with $L_x = 104.719$ is shown.
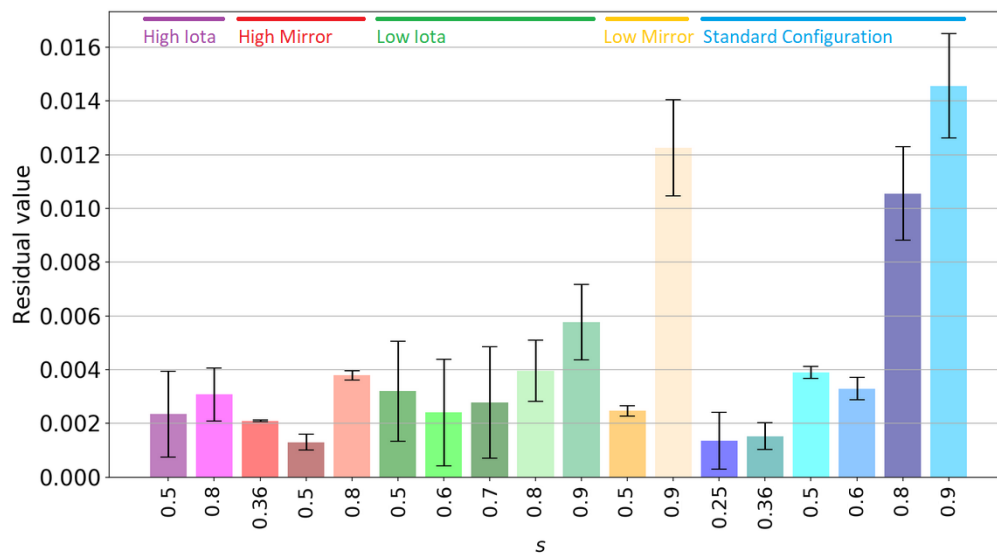

Figure A.1: Residual values for each data set with $L_x = 104.719$.

Table A.1: Residual values for each data set.

Number	Configuration	s	L_x	Residual
1	hi	0.5	104.719	0.002 ± 0.002
2	hi	0.5	110.997	0.003 ± 0.002
3	hi	0.5	665.979	0.00010 ± 0.00004
4	hi	0.8	104.719	0.003 ± 0.001
5	hm	0.36	104.719	0.00209 ± 0.00003
6	hm	0.36	530.418	0.003 ± 0.002
7	hm	0.5	104.719	0.0013 ± 0.0003
8	hm	0.5	310.957	0.0007 ± 0.0008
9	hm	0.5	621.914	0.002 ± 0.002
10	hm	0.8	78.832	0.0067 ± 0.0006
11	hm	0.8	104.719	0.0038 ± 0.0002
12	hm	0.8	266.000	0.0020 ± 0.0004
13	hm	0.8	530.000	0.002 ± 0.001
14	li	0.5	104.719	0.003 ± 0.002
15	li	0.5	340.925	0.0015 ± 0.0005
16	li	0.5	681.850	0.0003 ± 0.0003
17	li	0.6	104.719	0.002 ± 0.002
18	li	0.7	104.719	0.003 ± 0.002
19	li	0.8	90.837	0.0144 ± 0.0002
20	li	0.8	104.719	0.004 ± 0.001
21	li	0.9	104.719	0.006 ± 0.001
22	lm	0.5	104.719	0.0025 ± 0.0002
23	lm	0.5	136.837	0.004 ± 0.001
24	lm	0.5	684.184	0.0007 ± 0.0005
25	lm	0.9	104.719	0.012 ± 0.002
26	sd	0.25	104.719	0.001 ± 0.001
17	sd	0.25	774.957	0.0001 ± 0.0001
28	sd	0.36	104.719	0.0015 ± 0.0005
29	sd	0.36	436.870	0.0001 ± 0.0001
30	sd	0.5	104.719	0.0039 ± 0.0002
31	sd	0.5	130.316	0.0014 ± 0.0008
32	sd	0.5	260.633	0.0002 ± 0.0002
33	sd	0.5	621.914	0.00013 ± 0.00009
34	sd	0.6	104.719	0.0033 ± 0.0004
35	sd	0.6	138.185	0.0012 ± 0.0008
36	sd	0.6	198.992	0.0003 ± 0.0003
37	sd	0.8	68.805	0.017 ± 0.002
38	sd	0.8	95.562	0.012 ± 0.002
39	sd	0.8	104.719	0.011 ± 0.002
40	sd	0.8	137.610	0.007 ± 0.001
41	sd	0.9	59.952	0.027 ± 0.001
42	sd	0.9	104.719	0.015 ± 0.002

Zonal flow decay time

The zonal flow decay time is defined as $\tau_{ZF} = \int_0^{\tau_f} \mathcal{R}_{\|_\S}(t)dt$, with τ_f the time at which the residual value is reached. This integral is taken as well over the normalized imaginary parts of ϕ. The results are shown in figure A.2.

The zonal flow decay time for all data with $L_x = 104.719$ is shown in figure A.3. The integrals over $\text{Re}[\phi(t)/\phi(0)]$ for all data with $L_x = 104.719$ are shown in figure A.4.
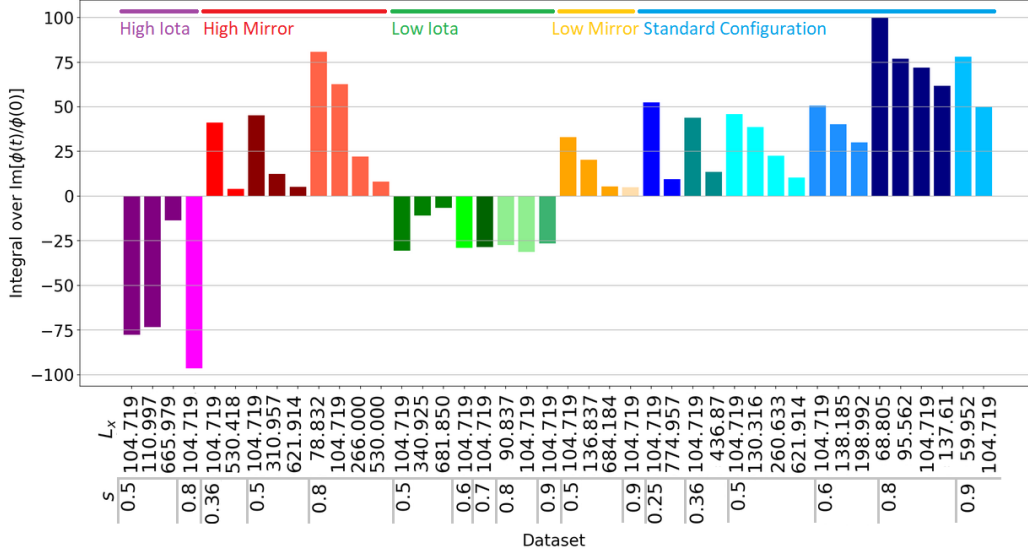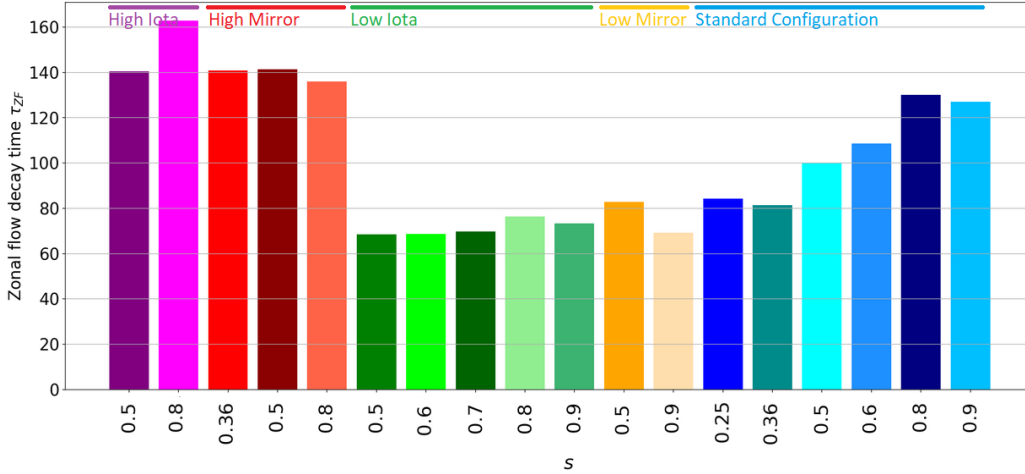

Figure A.2: Integral over $\text{Im}[\phi(t)/\phi(0)]$ for each data set.

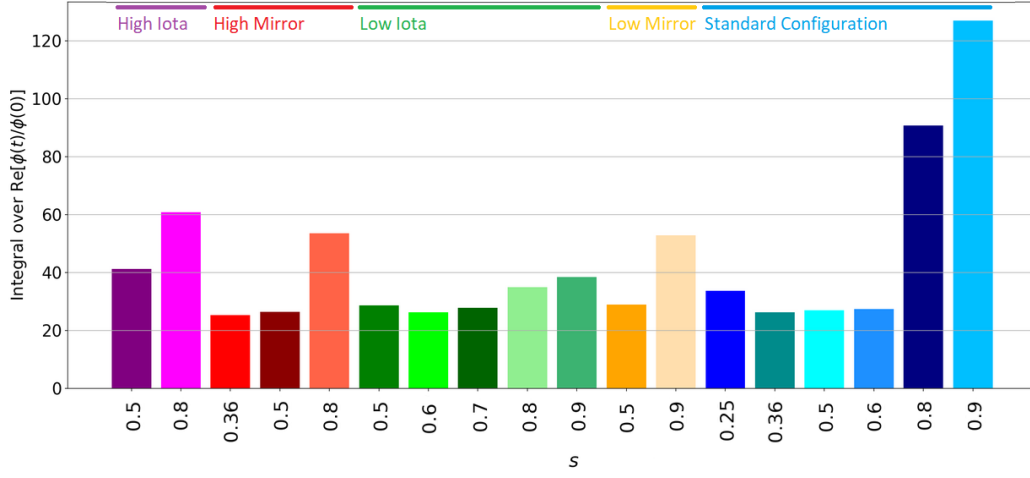Figure A.3: Zonal flow decay time for all data with $L_x = 104.719$.

Figure A.4: Integral over $\mathrm{Re}[\phi(t)/\phi(0)]$ for all data with $L_x = 104.719$.
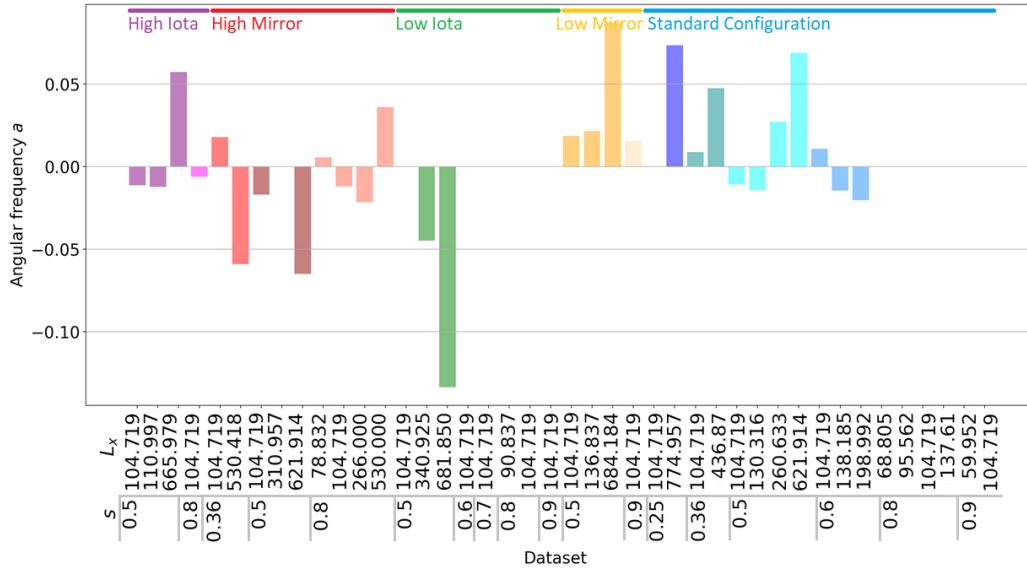
Decay constant

Figure A.5: Angular frequencies a determined by the fitting function for each data set. The angular frequency of dataset 8 is left out.

In figure A.6 the decay constant determined by the fitting function $y(t) = \cos{(at)}\exp{(-bt)}$ for all data sets with $L_x = 104.719$ is shown.
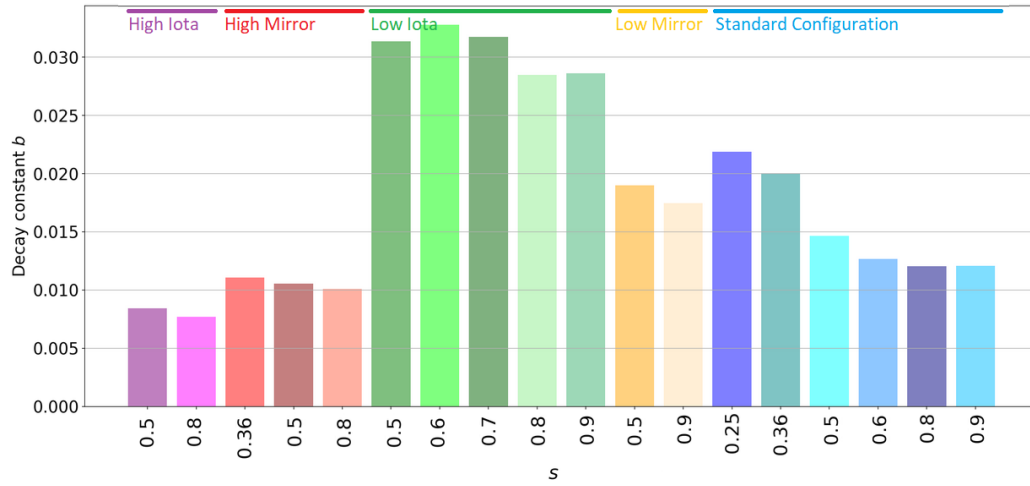
Figure A.6: Decay constant determined by the fitting function $y(t) = \cos{(at)} \exp{(-bt)}$ for all data sets with $L_x = 104.719$.